Contents lists available at ScienceDirect

Agricultural and Forest Meteorology
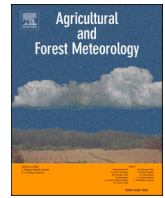
A coupled equilibrium boundary layer model with stable water isotopes and its application to local water recycling

Ke Xiao [a,*], Timothy J. Griffis [a], Xuhui Lee [b], Wei Xiao [c], John M. Baker [a,d]

[a] *Department of Soil, Water, and Climate, University of Minnesota, Twin Cities, Saint Paul, MN, USA*
[b] *School of the Environment, Yale University, New Haven, CT, USA*
[c] *Yale-NUIST Center on Atmospheric Environment & Jiangsu Collaborative Innovation Center of Atmospheric Environment and Equipment Technology, Nanjing University of Information Science & Technology, Nanjing, China*
[d] *USDA-ARS Soil and Water Research Unit, Saint Paul, MN, USA*

ABSTRACT

The contribution of evapotranspiration (ET) to regional precipitation, known as "local water recycling", is a key process in the water cycle that can affect water management. However, the amount of planetary boundary layer (PBL) moisture that arises from ET is highly uncertain due to complex atmosphere and land surface conditions. In this study, an idealized two-layer equilibrium boundary layer model was coupled with a stable water isotope module including HDO and $H_2^{18}O$ to constrain PBL growing season water transport processes. The model was validated using turbulent heat fluxes and isotope ratios of water vapor (δ_m) and precipitation (δ_P) measured at a cropland site and a nearby tall tower in the Upper Midwest, United States. The results show that the PBL equilibrium features of δ_m and δ_P are well-constrained by thermal and moisture equilibrium in the PBL. For this study region, the summer values of rain evaporation fraction (f) and local water recycling ratio (LRR) are estimated to be 0.09 and 0.29 ± 0.12, respectively. The summer LRR values for the years 2006–2010 were 0.35, 0.36, 0.17, 0.29, and 0.29, respectively. The small value of LRR in 2008 corresponded to a drought condition with the lowest precipitation and second lowest ET among the five years. The summer magnitude of the amount effect is $-2.8‰$ (mm day^{-1})$^{-1}$ and $-0.8‰$ (mm day^{-1})$^{-1}$ for HDO and $H_2^{18}O$, respectively. The local water recycling is identified as a significant factor influencing the continental isotope effect. Cropland has likely changed the regional LRR by -7.6 to 19.5% under different pre-agriculture land use scenarios. The feedback processes revealed here indicate that local water recycling is expected to be weakened under drought conditions, but it will be enhanced if irrigation is applied more intensely with more frequent drought events as the climate continues to warm.

1. Introduction

Evapotranspiration (ET) is a dominant moisture source in the planetary boundary layer (PBL) affecting the terrestrial water cycle (Oki and Kanae, 2006; Wang and Dickinson, 2012). The contribution of ET to regional precipitation, known as "local water recycling", is a key mechanism that affects the water cycle and water management (Keys et al., 2019; Trenberth, 1999; Van Der Ent and Savenije, 2011). On global average, the ratio of precipitation over land originating from terrestrial ET, the "recycling ratio", is about 40% (Van Der Ent et al., 2010). However, the contribution of ET to precipitation is highly uncertain at the regional scale.

ET is affected by multiple factors, including meteorological variables (such as air temperature, air moisture, wind speed, and radiation) and land surface characteristics (such as canopy resistance, surface roughness, and albedo) (Haghighi and Kirchner, 2017; McVicar et al., 2012). The water cycle is expected to be intensified in response to global warming (Durack et al., 2012; Huntington, 2006; Santer et al., 2007). Land surface characteristics are changing due to agricultural intensification and other land use changes. For example, the grass-to-corn/soy conversion rate was 1.0–5.4% annually across the western Corn Belt, United States (US) over the period 2006–2012 (Wright and Wimberly, 2013). Such changes in climate and land-use can drive important shifts in ET (Alter et al., 2018), and may significantly alter the magnitude and patterns of local water recycling (te Wierik et al., 2021; Van Der Ent et al., 2014; Zeng et al., 2018).

Tracing the stable hydrogen and oxygen isotopes in water is a powerful way to study hydrometeorological processes in the soil-plant-atmosphere continuum. The variations of isotope concentrations provide additional information that can reveal the underlying controls on water cycle processes, such as ET partitioning, rain evaporation, local water recycling, and water sources of precipitation (Griffis et al., 2016; Werner et al., 2012; Worden et al., 2007). The isotope ratios of HDO/H$_2$O and H$_2^{18}$O/H$_2^{16}$O (traditionally presented as δD and δ^{18}O, respectively) in water vapor record the condensation and evaporation history of an air mass (Lee et al., 2005; Worden et al., 2007). For example, Craig and Gordon (1965) proposed a model of evaporation, mixing, and precipitation condensation over the ocean that considered isotope fractionation effects. Worden et al. (2007) compared HDO observations from the Tropospheric Emission Spectrometer (TES) on the Aura spacecraft with process curves of simple isotope models and found that ET is an important source that enriches the water vapor over continents. Isotope observations can also be used to partition ET into evaporation and transpiration, as the transpired vapor is typically more enriched in heavy isotopes than the soil evaporated vapor (Wang et al., 2010; Xiao et al., 2018; Yakir and Wang, 1996).

The isotope ratios, δD and δ^{18}O, found in global precipitation observations are generally linearly correlated, following the Global Meteorological Water Line (GMWL), where δD $= 8\delta^{18}$O $+ 10‰$ (Craig, 1961). The slope of 8 is determined by the Rayleigh distillation process. Here, ET and rain evaporation can drive the values of δD and δ^{18}O off the GWML (Dansgaard, 1964). Consequently, the deuterium excess, which is defined as $d = \delta$D $- 8\delta^{18}$O, can also reveal how local hydrometeorological processes influence the water cycle. For example, Lai and Ehleringer (2011) found a diurnal cycle of deuterium excess of water vapor over a coniferous forest with the maximum in the early morning and the minimum around noon, indicating that ET was the primary moisture source in the mid-afternoon PBL. In a global meta-analysis, Welp et al. (2012) found similar diurnal patterns of deuterium excess. Observations of deuterium excess indicate that the isotope composition of water vapor in the PBL is also driven by the solar radiative forcing at the diurnal scale (Lee et al., 2012).

Multiple idealized equilibrium PBL models have revealed that the diurnal averages of the PBL features (such as ET, potential temperature and specific humidity) display a long-term equilibrium with timescales longer than a month in response to the solar radiative forcing (e.g. Betts, 2000; Betts et al., 2004; McColl et al., 2019; Raupach, 2000). For example, Betts (2000) developed an idealized one-layer equilibrium boundary layer model over land, showing a quasi-linear response between the mixed layer (ML) height and the equilibrium specific humidity. Betts et al. (2004) extended the one-layer model into a two-layer PBL model by adding a cloud layer, or the convective boundary layer (CBL) above the ML. The two-layer model showed reasonable equilibrium concentrations of carbon dioxide and radon in the ML. Since the isotope ratios of water vapor in the ML show a well-mixed vertical profile (Bony et al., 2008; Lee et al., 2012) and pronounced diurnal variation (Lai and Ehleringer, 2011; Welp et al., 2012), the equilibrium boundary layer model should reveal the long-term equilibrium of the isotope compositions of water vapor in the PBL. Furthermore, the changes in the hydrometeorological processes, such as ET and local water recycling, are expected to alter the PBL equilibrium values of the water vapor isotope composition.

In this study, we coupled a water isotope module to the idealized equilibrium boundary layer model of Betts (2000) and Betts et al. (2004) (abbreviated as B00 and B04, respectively) to solve for the equilibrium values of oxygen and hydrogen isotope compositions of the water vapor and the water cycle components (e.g., ET, entrainment, and precipitation) within the PBL. We applied this modeling approach in the Upper Midwest US for the growing season to investigate the equilibrium isotope composition of water vapor in the PBL and the local water recycling within the region. The main objectives were to: (1) identify the long-term (seasonal and interannual) equilibrium of surface turbulent fluxes and isotope composition of water vapor in the ML; (2) use this modeling approach with observations to constrain the rain evaporation fraction and local water recycling ratio; and (3) explore the changes of isotope composition equilibrium and local water recycling affected by different vegetation types (broadleaf forest, needleleaf forest, grassland, and cropland).

This paper is organized as follows: First, the model equations are introduced; second, the model is validated using the *in-situ* observations at a cropland site; third, the sensitivity analyses for five parameters are shown to verify that the model parameters are well-constrained, to quantify the rain evaporation fraction and local water recycling ratio, and to model the isotope amount effect and continental effect; fourth, model results derived for different land surface scenarios are used to examine the influence of croplands on the local water recycling in the Upper Midwest US; and finally, the potential model applications for regional climate and isotope studies are discussed.

2. Model description

The model consists of a base model and a coupled water isotope module. The base model is mainly established using the two-layer framework of B04, defining the climate background with components including surface energy balance, thermal equilibrium in the ML, moisture equilibrium in the ML and the CBL. The water isotope module uses the equilibrium solutions of the base model to solve for the mass mixing ratio equilibrium of HDO and H$_2^{18}$O in the ML and the CBL. While the original B04 framework only considers the non-precipitation condition, the base model includes the precipitation-related processes such as condensation, rain evaporation and local water recycling (Fig. 1). The major modifications include: (1) using the observed precipitation and rain evaporation fraction to quantify the parameter of rain evaporation cooling rate originally from B00 and applying the cooling rate to the thermal equilibrium of B04; (2) adding rain evaporation and condensation to the moisture equilibrium of B04; and (3) partitioning the moisture source of precipitation into local ET and advection above the PBL to determine the local water recycling ratio, with the idealized assumption that advection occurs above the PBL and is omitted within the PBL.

2.1. Base model

2.1.1. Surface energy balance

At the land surface, the net available energy (Q) is the difference between the net radiation (R_n) at the canopy top and the ground heat flux (G), which is equal to the sum of the turbulent heat fluxes, i.e. the sum of sensible heat flux (H_0) and latent heat flux (LE_0):

$$Q = R_n - G = H_0 + LE_0, \tag{1}$$

where $L = 2.5 \times 10^6$ J kg^{-1} is the specific latent heat of water vaporization, and E_0 is the surface evapotranspiration.

2.1.2. Thermal equilibrium in the ML

Following B00 and B04, we consider the thermal equilibrium in the ML and ignore the thermal status above the ML top. The three thermal terms include the surface sensible heat flux (H_0), thermal entrainment between the ML and the CBL (H_b), and the cooling term, consisting of radiative cooling (F_{rad}) and rain evaporation cooling (F_{evap}); these are balanced in the ML:

$$C_p \left(\frac{P_{LCL}}{g} \right) \frac{\partial \theta_m}{\partial t} = \left(\frac{\theta_0}{T_0} \right) H_0 - \left(\frac{\theta_b}{T_b} \right) H_b + \left(F_{rad} + F_{evap} \right) = 0. \tag{2}$$

Here, P_{LCL} is the height of the ML top in pressure coordinates (values increase from zero at the ground surface), which is assumed to be identical to the pressure height of the lifting condensation level (LCL) and the cloud base suggested by B00 and B04. The variables T and θ are
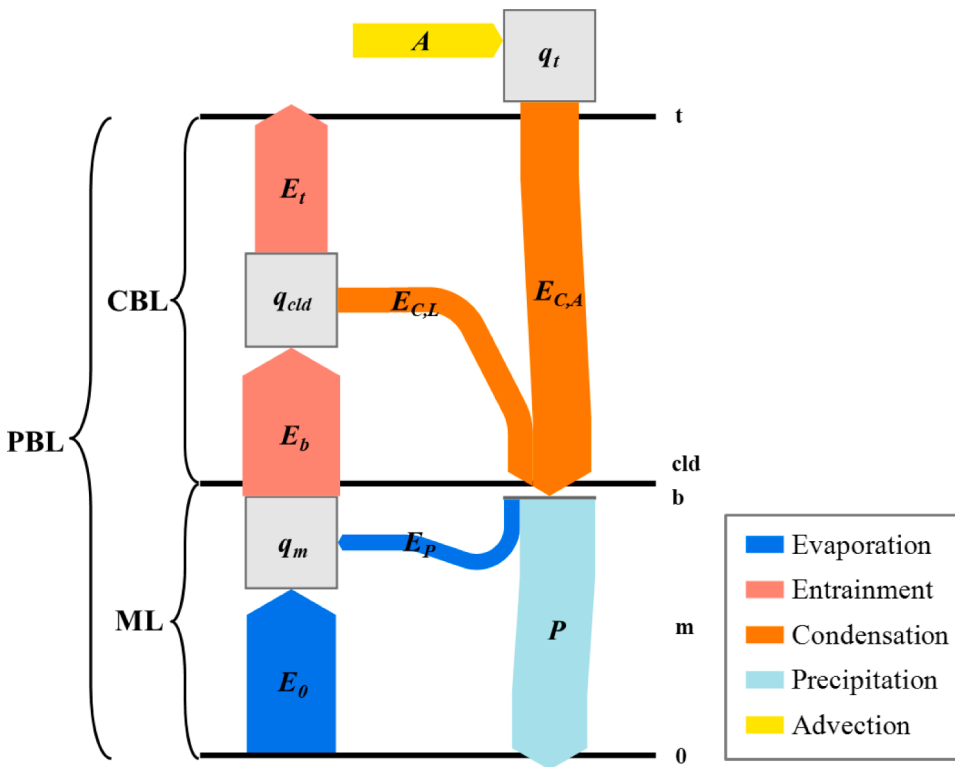
Fig. 1. Framework of moisture fluxes in the two-layer equilibrium planetary boundary layer (PBL) model. The components are evapotranspiration (E_0), entrainment at the mixed layer (ML) top (E_b), entrainment at the convective boundary layer (CBL) top (E_t), condensation from local moisture ($E_{C,L}$), condensation from advected moisture ($E_{C,A}$), precipitation to the ground (P), rain evaporation (E_P), and advection above the PBL (A). The variable q is specified humidity. The subscripts 0, m, b, cld, and t represent the surface, mixed layer, the top of mixed layer, cloud base, and the top of PBL, respectively.

temperature and potential temperature, respectively. The subscripts 0, m, and b represent the surface, ML, and cloud base, respectively. The value of specific heat capacity of air (C_p) is 1005 J kg^{-1} K^{-1}, and the gravitational acceleration (g) is 9.8 m s^{-2}.

The surface sensible heat flux is determined by the bulk aerodynamic approach in B00 and B04:

$$H_0 = \rho_0 C_p r_a^{-1}(T_0 - T_m),$$ (3)

where ρ_0 is the surface air density, and r_a is the aerodynamic resistance of air. Here, $r_a = c_a U^{-1}$, where $c_a = 100$ is set as a constant aerodynamic transfer coefficient ignoring atmospheric stability; and U is the 2-m horizontal wind speed above the canopy. T_0 is the surface temperature and T_m is the 2-m air temperature above the canopy.

The thermal mixing between the ML and the CBL (H_b) is the product of entrainment mass flux ($\rho_b W_b$) and the potential temperature difference ($\theta_{cld} - \theta_m$) of the two layers (B04):

$$\left(\frac{\theta_b}{T_b}\right) H_b = -\rho_b W_b C_p(\theta_{cld} - \theta_m),$$ (4)

where W_b is the entrainment velocity at the cloud base; θ_{cld} is the potential temperature at the bottom of the cloud layer; θ_m is the potential temperature in the ML; and θ_b and T_b are the potential temperature and air temperature at the cloud base, respectively.

The radiative cooling (F_{rad}) is determined by the radiative cooling rate ($\partial\theta_{rad}/\partial t < 0$), which is set as a prescribed parameter in the model:

$$F_{rad} = C_p \left(\frac{P_{LCL}}{g}\right) \frac{\partial\theta_{rad}}{\partial t}.$$ (5)

The rain evaporation cooling (F_{evap}) is equivalent to the latent heat absorbed by the rain evaporation (E_P):

$$F_{evap} = C_p \left(\frac{P_{LCL}}{g}\right) \frac{\partial\theta_{evap}}{\partial t} = -LE_P.$$ (6)

Therefore, the rain evaporation cooling rate ($\partial\theta_{evap}/\partial t < 0$) is determined by the mass flux of rain evaporation (E_P) and the height of the ML (P_{LCL}):

$$\frac{\partial\theta_{evap}}{\partial t} = -\frac{Lg}{C_p P_{LCL}} E_P.$$ (7)

2.1.3. Moisture equilibrium in the ML

In the ML, the change rate of specific humidity (dq_m/dt) is determined by the moisture fluxes of surface ET (E_0), entrainment at the ML top (E_b) and rain evaporation (E_P). In the equilibrium state, the change rate of q_m is zero and the three flux terms are in balance:

$$\left(\frac{P_{LCL}}{g}\right) \frac{dq_m}{dt} = E_0 - E_b + E_P = 0.$$ (8)

Using the aerodynamic approach from B00 and B04, the surface ET is given as:

$$E_0 = \rho_0(r_a + r_c)^{-1}(q_s(T_0) - q_m),$$ (9)

where $q_s(T_0)$ is the saturation specific humidity near the soil surface, q_m is the equilibrium specific humidity in the ML and r_c is the canopy resistance. The model uses r_c as the independent variable.

Entrainment between the ML and the CBL is the product of entrainment mass exchange ($\rho_b W_b$) and moisture difference ($q_{cld} - q_m$) of the two layers (B04); and ρ_b and W_b are the cloud-base air density and subsidence velocity, respectively:

$$E_b = -\rho_b W_b(q_{cld} - q_m).$$ (10)

We assume that rain evaporation only occurs in the ML:

$$E_P = f\frac{P}{1-f},$$ (11)

where f is the fraction of rain evaporation, P is the precipitation rate measured at the ground level, and $P/(1-f)$ is the total condensed rainwater.

2.1.4. Moisture equilibrium in the CBL

B04 suggested that the growth and subsidence of the CBL are balanced by entrainment, and therefore a long-term equilibrium in the CBL is maintained. For the CBL moisture equilibrium, the change rate of specific humidity in the CBL (dq_{cld}/dt) is zero with the balance among entrainment at the ML top (E_b), entrainment at the CBL top (E_t), and rainwater condensation (E_C):

$$\left(\frac{P_{CL}}{g}\right)\frac{dq_{cld}}{dt} = E_b - E_t - E_C = 0, \tag{12}$$

where P_{CL} is the pressure depth of the cloud layer, or the CBL, defined as the pressure height difference between the CBL top and the ML top ($P_{CBL} - P_{LCL}$). Here, we follow the B04 assumption that the pressure height of the CBL top (P_{CBL}), or the PBL top as well, is 350 hPa (i.e. the pressure level of the CBL top is 350 hPa lower than the surface pressure, or typically 3500 m altitude above sea level).

B04 assumes a constant subsidence rate ($\rho_t W_t$) in the CBL. Our model follows this assumption and partitions the water vapor entrained from the ML to the CBL (E_b) into the condensation in the CBL (E_C) and the entrainment to the upper free atmosphere above the PBL (E_t):

$$E_b = E_t + E_C = -\rho_t W_t (q_t - q_m), \tag{13}$$

where $\rho_t W_t$ is the entrainment mass exchange in the CBL, and q_t is the boundary condition prescribed by the specific humidity in the free atmosphere.

2.1.5. Local water recycling ratio

The total precipitated water to the ground (P) is ideally divided into two parts: the precipitation contributed by local ET (P_L) and the precipitation from free-atmosphere advection (P_A):

$$P = P_L + P_A, \tag{14}$$

where the subscripts L and A represents the local and advected components, respectively.

The condensation in the CBL (E_C) resulting from local ET ($E_{C,L}$) is described as:

$$E_C = E_{C,L} = \frac{P_L}{1-f}. \tag{15}$$

The condensation from the free-atmosphere advected water is described as:

$$E_{C,A} = \frac{P_A}{1-f}. \tag{16}$$

The local water recycling ratio (LRR) is defined as the ratio of local precipitation to the total precipitation (Van Der Ent et al., 2014):

$$LRR = \frac{P_L}{P}. \tag{17}$$

In the model, LRR is set as an input parameter. However, it will be shown later in the sensitivity analyses that LRR can be constrained with observations of ET and isotope ratios by the model-generated sensitivity diagrams. P_L can be determined from the observed total precipitation as $P_L = LRR \cdot P$.

2.1.6. Closure scheme

Following B00 and B04, three upper boundary conditions at the ML top are necessary closures that are applied to solve the base model. These include the potential temperature at the cloud base, the relative humidity at the cloud base, and the virtual heat flux at the ML top. These three closures are described in Section S2.1 in the supplemental material.

2.2. Water isotope module

After solving the base model, the equilibrium solutions of temperature and mass mixing ratio of water vapor for each layer were used to drive the water isotope module. To be consistent with the units in the base model, we express the heavy isotope fluxes and concentrations in terms of mass fluxes and mass mixing ratios, respectively. The equation forms of the hydrogen and oxygen isotopes are identical, except for the values of their fractionation factors. Here, we present the isotope terms with a subscript i to represent either HDO or $H_2^{18}O$.

2.2.1. ML equilibrium

In the ML, the change rate of water isotope mass mixing ratio ($dq_{i,m}/dt$) is determined by the mass fluxes of surface ET ($E_{i,0}$), entrainment at the ML top ($E_{i,b}$) and rain evaporation ($E_{i,P}$). In equilibrium, the three terms are balanced:

$$\left(\frac{P_{LCL}}{g}\right)\frac{dq_{i,m}}{dt} = E_{i,0} - E_{i,b} + E_{i,P} = 0. \tag{18}$$

The isotope mass flux of ET over a canopy is presented in aerodynamic form with a kinetic fractionation factor (Worden et al., 2007):

$$E_{i,0} = \rho_0 \eta_i (r_a + r_c)^{-1} \left(\frac{R_0}{\alpha(T_0)}\frac{M_i}{M_w}q_s(T_0) - q_{i,m}\right), \tag{19}$$

where η_i is the kinetic fractionation factor related to the differences in isotopic molecular diffusivity ratios (Merlivat & Jouzel, 1979; Cappa et al., 2003). R_0 is the isotope molar ratio of soil water at the surface, which is a specified boundary condition; α is the liquid-vapor equilibrium fractionation factor ($\alpha > 1$) depending on temperature (Horita and Wesolowski, 1994), and $R_0/\alpha(T_0)$ is the isotope molar ratio of vapor just above the surface. M_i/M_w is a factor converting molar ratio to mass mixing ratio, where M_i is the molecular weight of HDO or $H_2^{18}O$ and M_w is the molecular weight of H_2O.

Entrainment is assumed to mix air completely without a fractionation effect. Therefore, we can use a similar parameterization in the PBL model to represent the water isotope mixing at the ML top:

$$E_{i,b} = -\rho_b W_b (q_{i,cld} - q_{i,m}). \tag{20}$$

2.2.2. CBL equilibrium

Similar to the water vapor mixing ratio in the CBL, the isotope fluxes are balanced by entrainment at the ML top ($E_{i,b}$), entrainment at the CBL top ($E_{i,t}$), and condensation ($E_{i,C}$):

$$\left(\frac{P_{CL}}{g}\right)\frac{dq_{i,cld}}{dt} = E_{i,b} - E_{i,t} - E_{i,C} = 0. \tag{21}$$

The entrainment at the cloud base ($E_{i,b}$) is divided into the condensation ($E_{i,C}$) in the CBL and the entrainment to the free atmosphere above the PBL ($E_{i,t}$) as:

$$E_{i,b} = E_{i,t} + E_{i,C} = -\rho_t W_t (q_{i,t} - q_{i,m}), \tag{22}$$

where the isotope mixing ratio above the PBL ($q_{i,t}$) is the boundary condition determined by the prescribed isotope ratio above the PBL (δ_t).

Worden et al. (2007) suggested the isotope condensation term as αRC, where α is the temperature-dependent equilibrium fractionation factor ($\alpha > 1$), R is the isotope molar ratio, and C is the condensation rate. Therefore, the isotope mass flux of the CBL condensation is given by:

$$E_{i,C} = E_{i,C,L} = \alpha(T_{CL})E_{C,L}\frac{E_{i,0}}{E_0}, \tag{23}$$

where T_{CL} is the average temperature of the CBL, which is equivalent to the temperature at the middle of the CBL while assuming a constant temperature lapse rate Γ (See Eq. S1).

The isotope mass flux of the free-atmosphere condensation is given as:

$$E_{i,C,A} = \alpha(T_t) E_{C,A} \frac{q_{i,t}}{q_t}, \tag{24}$$

where the specific humidity (q_t) and the isotope mass mixing ratios ($q_{i,t}$) above the PBL are prescribed and assumed to be identical to the advected water vapor. The temperature at the PBL top (T_t) is calculated from potential temperature (θ_t) derived from Eq. S1 with $P_{CBL} = 350$ hPa.

2.2.3. Isotope composition of precipitation and rain evaporation

According to Worden et al. (2007), the isotope mass flux of the rain evaporation can be calculated by:

$$E_{i,P} = E_{i,P,L} + E_{i,P,A} = \frac{f}{\alpha_e(T_{ML})} \left(E_{i,C,L} + E_{i,C,A} \right), \tag{25}$$

where f is the evaporated rain fraction, T_{ML} is the average temperature of the ML, and α_e (>1) is the kinetic fractionation factor accounting for molecular diffusive transport in the rain drops (Stewart, 1975).

Finally, the isotope mass mixing ratio in accumulated precipitation water is what remains in the condensed water after rain evaporation and is calculated as:

$$P_i = P_{i,L} + P_{i,A} = \left(E_{i,C,L} - E_{i,P,L} \right) + \left(E_{i,C,A} - E_{i,P,A} \right)$$
$$= \left(E_{i,C,L} + E_{i,C,A} \right) \left(1 - \frac{f}{\alpha_e(T_{ML})} \right). \tag{26}$$

2.3. Iterative process

The input parameters and variables to drive the model are listed in Table 1 and described in Section 3.1. The base model and the water isotope module were solved by iteration in two steps. First, in the base model, a range of r_c values were given as the independent variable, other variables such as P_{LCL}, θ_m, q_m, θ_{cld}, q_{cld}, and subsidence (i.e. $\rho_t W_t$ and $\rho_b W_b$) were solved at each value of r_c iteratively. Second, these solved meteorological equilibrium states were passed to the water isotope module to solve the equilibrium states of the isotope mass mixing ratios, such as $q_{D,m}$, $q_{D,cld}$, $q_{18O,m}$, and $q_{18O,cld}$. Finally, we have expressed the isotope compositions in the familiar delta (δ) notation as:

$$\delta(‰) = \left(\frac{R}{R_{std}} - 1 \right) \times 1000, \tag{27}$$

where $R = (q_i M_i^{-1})/(q M_w^{-1})$ is the molar ratio of the less abundant over the more abundant isotopic species and R_{std} is a standard molar ratio corresponding to the Vienna Standard Mean Ocean Water (VSMOW) scale, which is 311.5 ppm for HDO/H$_2$O and 2005.2 ppm for H$_2^{18}$O/H$_2^{16}$O.

2.4. Model limitations

First, consistent with the models of B00 and B04, the equilibrium model applied here is an idealized model that represents a climate average of the daily mean boundary layer over a long-term period (monthly or longer timescales). The atmosphere may not be strictly in equilibrium on the 24-hour timescale. However, the average of the day-to-day variation should approach a climate equilibrium provided that the long-term atmospheric thermal and moisture conditions are in balance. We note that the model is not expected to explain variations at the daily or sub-daily timescales.

Second, for some parameter settings, the model will not converge to a solution during iteration. This implies a non-equilibrium condition. For example, at very low r_c values, the model will not converge to a solution. Here, the sensible heat flux is too strong to maintain the equilibrium at the low PBL height.

Finally, there are limitations with the simplified assumptions in the model. For example, advection below the PBL top is ignored, which could influence the background isotope composition (Worden et al., 2007). The microphysical processes in cloud and precipitation are largely simplified, which might potentially affect the isotope equilibrium. For instance, the rainwater formation only considers the vapor-liquid phase changes in condensation and ignores the ice phase. However, we note that ice-phase processes can be important in summertime precipitation associated with deep convection (Fu and Qin, 2014; Mülmenstädt et al., 2015). Furthermore, the model does not separate the convective precipitation and large-scale stratiform precipitation, while rainwater in convective precipitation tends to be more enriched (Aggarwal et al., 2016). Despite these simplifications, the model can capture some essential isotope features of ET, precipitation, and local water recycling during summer and can provide valuable insights regarding the interpretation of the isotope composition of atmospheric water vapor and precipitation.

3. Materials and methods

3.1. Model parameters

The study site for model setup and validation is the AmeriFlux core site US-Ro1 (44°42′52″N, 93°5′23″W, 260 m above sea level), which is a corn-soybean rotation cropland located in Rosemount, MN (Baker & Griffis, 2005). The model was run and validated for summer seasons (June to August), because the model only considers the vapor-liquid phase changes in condensation and precipitation.

Table 1

Reference parameters for the base model and parameter ranges for sensitivity tests.

Parameter	Source	Reference	Range	Unit
Conceptual parameters of base model				
Canopy resistance r_c	–	60 to 900	60 to 900	s m^{-1}
Radiative cooling rate $\partial\theta_{rad}/\partial t$	B00	−2	–	K day^{-1}
Entrainment parameter k	B00/B04	0.2	–	–
Stability Γ	B00/B04	0.06	–	K hPa^{-1}
Pressure height of the CBL top P_{CBL}	B04	350	–	hPa
Meteorological variables				
Net available energy Q	US-Ro1	138	–	W m^{-2}
Surface pressure P_o	US-Ro1	980	–	hPa
Aerodynamic resistance $r_a = 100 U^{-1}$ (U, wind speed)	US-Ro1	51.5	–	s m^{-1}
Reference potential temperature θ_{ref}	MPX	295	–	K
Precipitation rate P	US-Ro1	3.3	–	mm day^{-1}
Precipitation parameters				
Rain evaporation fraction f	–	0.1	0 to 0.4	–
Local water recycling ratio LRR	–	0.3	0 to 1	–
Kinetic fractionation factors				
η_D	–	0.9892	–	–
η_{18O}	–	0.9930	–	–
Boundary variables above the PBL				
q_t	TES	3.2	–	g kg^{-1}
δD_t	TES	−160	−100 to −200	‰
$\delta^{18}O_t$	–	−23.1	−10 to −30	‰
Boundary variables at the surface				
δD_o	US-Ro1	−50	−30 to −80	‰
$\delta^{18}O_o$	US-Ro1	−5	−2.5 to −10	‰

A group of reference parameters and variables were prescribed to define a climate normal for the base model and the water isotope module (Table 1). The conceptual parameters in the base model such as radiative cooling rate, entrainment parameter, stability, reference potential temperature and pressure height of the CBL top were determined following B00 and B04 (see supplemental material Section S2.1). The input meteorological variables, such as net available energy, surface pressure, aerodynamic resistance (calculated from wind speed) and precipitation, were the ensemble averages of the summer observations at US-Ro1 from June to August 2004–2012 (Table S1). Both the rain evaporation fraction and the local recycling ratio are tunable parameters in the model. The reference value of rain evaporation fraction was arbitrarily prescribed as 0.1. The reference value of local recycling ratio was set as 0.3 according to previous studies in the same region (Griffis et al., 2016). We will assess if these two parameters are well constrained by comparing them with the results from the model sensitivity tests. The kinetic fractionation factors of evaporation (η_D and η_{18O}) in Eq. (19) were tuned and determined by model validation.

For the boundary conditions, the base model only needs the specific humidity above the PBL (q_t), while the isotope module requires isotope ratios of HDO and $H_2^{18}O$, both above the PBL (δD_t and $\delta^{18}O_t$) and at the surface (δD_0 and $\delta^{18}O_0$) (Table 1). The values of q_t and δD_t were both retrieved from the Tropospheric Emission Spectrometer (TES) Level 3 daily products on the Aqua satellite (Beer et al., 2001; Worden et al., 2006). The reference values were the average summer measurements of the grid point nearest to US-Ro1 at the pressure level of 680 hPa in the TES product from 2005 to 2011. Since TES did not measure the profile of $H_2^{18}O$, $\delta^{18}O_t = -23.1‰$ was calculated from $\delta D_t = -160‰$ by assuming a deuterium excess of 25‰, which was estimated by several summertime aircraft measurements at a similar latitude in the US (He and Smith, 1999). The summertime $\delta^{18}O_0$ in soil water at US-Ro1 was about $-5‰$ (Griffis et al., 2011; Welp et al., 2008), and δD_0 was set as $-50‰$ with the soil water line $\delta D = 5.3\delta^{18}O - 21.6$ at US-Ro1 (Griffis et al., 2016).

3.2. Data for model validation

Applying the same rationale as B00 and B04 in the model validation, the model outputs were compared with the climate equilibrium presented by the daily averaged observations. The base model was validated by the surface fluxes and the ML variables observed in June to August 2004–2012. The surface fluxes for validation were measured at US-Ro1 by the eddy covariance method following AmeriFlux standard protocols (Baker & Griffis, 2005). The potential temperature and specific humidity in the ML were averaged in the lowest 500 m of the sounding profiles from the MPX weather station (44°50′57″N, 93°33′53″W, 287 m above sea level) in Chanhassen, MN, which is about 40 km to the northwest of US-Ro1 (retrieved from http://weather.uwyo.edu/upperair/sounding.html). The sounding profiles were measured twice a day at 6:00 and 18:00 CST using weather balloons.

Although r_c is the independent variable in the model iteration, the results of model validation were typically presented with P_{LCL} as the x-axis. Compared with r_c, P_{LCL} is a more intuitive variable, which is more easily constrained by observations. Furthermore, the flux solutions are quasi-linearly correlated to P_{LCL} (Eq. S6). The observed P_{LCL} was calculated with sounding data as following (Betts, 1997):

$$P_{LCL} = \frac{1 - RH}{A + (A - 1)RH}P_0, \tag{28}$$

where $A = 0.622/(2C_pT)$, T is air temperature, RH is the relative humidity, and P_0 is the surface pressure. This empirical relation between RH and P_{LCL} generates similar results as Eq. S2 with errors less than 1%.

The water isotope module was validated by the isotope ratios of the ML and rainwater. The isotope ratios of water vapor in the ML were retrieved from the Stable Water Vapor Isotope Database (SWVID) (Wei et al., 2019). Both hydrogen and oxygen isotope compositions were

measured in summer 2010–2012 at a 244-m tall tower (44°41′19″N, 93°4′22″W; 290 m above sea level) in Rosemount, MN, which is 3 km away from US-Ro1 (Griffis et al., 2016). The water vapor was sampled at the height of 185 m and the isotope compositions were analyzed using a tunable diode laser (TGA200, Campbell Scientific Inc., Logan, UT, USA) (Griffis et al., 2016, 2010). The rainwater samples were collected in summer from 2006 to 2010 at a weather station on the Saint Paul Campus, University of Minnesota, which is 31.5 km north to US-Ro1 (Griffis et al., 2016) (Table S2). The isotope compositions of the samples were analyzed using a the Liquid Water Isotope Analyzer DLT-100 (Los Gatos Research Inc., Mountain View, CA, USA) following Schultz et al. (2011).

4. Results and discussion

4.1. Model validation

4.1.1. ML equilibrium of base model

The equilibrium solutions of the ML variables and the surface fluxes of the base model are compared with the linear regression of observations against P_{LCL} in Fig. 2. The modeled θ_m, q_m, H, and LE are all quasi-linearly correlated to P_{LCL}. Here, the linear regression is treated as a first guess of the "observed" climate equilibrium and used as a benchmark for model validation. The modeled equilibrium is considered closer to the observed equilibrium when the model line deviates less from the regression line within the range of model output (i.e. P_{LCL} is between 70 and 280 hPa).

Both observed and modeled θ_m increase with P_{LCL} with slopes of 0.0099 K hPa^{-1} ($p < 0.01$) and 0.054 K hPa^{-1}, respectively (Fig. 2a). The observed and modeled q_m are both negatively correlated to P_{LCL} with slopes of -0.043 (g kg^{-1}) hPa^{-1} ($p < 0.01$) and -0.020 (g kg^{-1}) hPa^{-1}, respectively (Fig. 2b). The slope of modeled θ_m is 5.4 times the observed trend, while the slope of modeled q_m is only half of the observation. Here we infer that the slope inconsistencies between model and observation reveal the disequilibrium condition in the soundings that were measured twice a day (i.e. weather soundings at 0600 and 1800 hr) and did not include hourly information of PBL development and diel dynamics. The measured soundings in early morning and late afternoon were less in equilibrium than noon and early afternoon. With PBL growth, the surface forcing warms and moistens the atmosphere less efficiently due to larger entrainment at the ML top, which causes flattened slopes in observed θ_m and steeper slopes in observed q_m compared with the modeled equilibrium condition.

The observed and modeled H are both positively correlated to P_{LCL}, with similar slopes of 0.20 (W m^{-2}) hPa^{-1} ($p < 0.01$) and 0.21 (W m^{-2}) hPa^{-1}, respectively (Fig. 2c), which indicates that the cooling terms are well-constrained (see Eq. S6). In the reference case, the radiative cooling rate is specified at -2 K day^{-1}, and the modeled rain evaporation cooling rate varies from -1.3 to -0.3 K day^{-1} as the PBL grows (Fig. S2). The magnitude of the rain evaporation cooling rate is about 15 to 65% of the radiative cooling rate, indicating that the radiative cooling is dominant on clear days with large PBL height and that the rain evaporation cooling will be more important on cloudy/rainy days with relatively small PBL height. This supports that rain evaporation is a key cooling process in the ML equilibrium as proposed by B00.

When P_{LCL} increases, the observed LE shows an increased trend with a slope of 0.11 (W m^{-2}) hPa^{-1} ($p < 0.01$), but the modeled LE declines with a slope of -0.21 (W m^{-2}) hPa^{-1} (Fig. 2d). The negative correlation between the modeled H and LE is consistent with the "surface flux equilibrium" (SFE) theory, which is a one-layer model for daily or monthly equilibrium H and LE over water-limited inland continental regions (McColl et al., 2019; McColl and Rigden, 2020). In SFE, when Q is fixed, a high H increases air temperature, induces a warmer atmosphere near the surface, and leads to declines in LE and surface moisture and *vice versa* for a low H situation. Therefore, LE determines the near-surface RH in the equilibrium condition, and the near-surface RH in
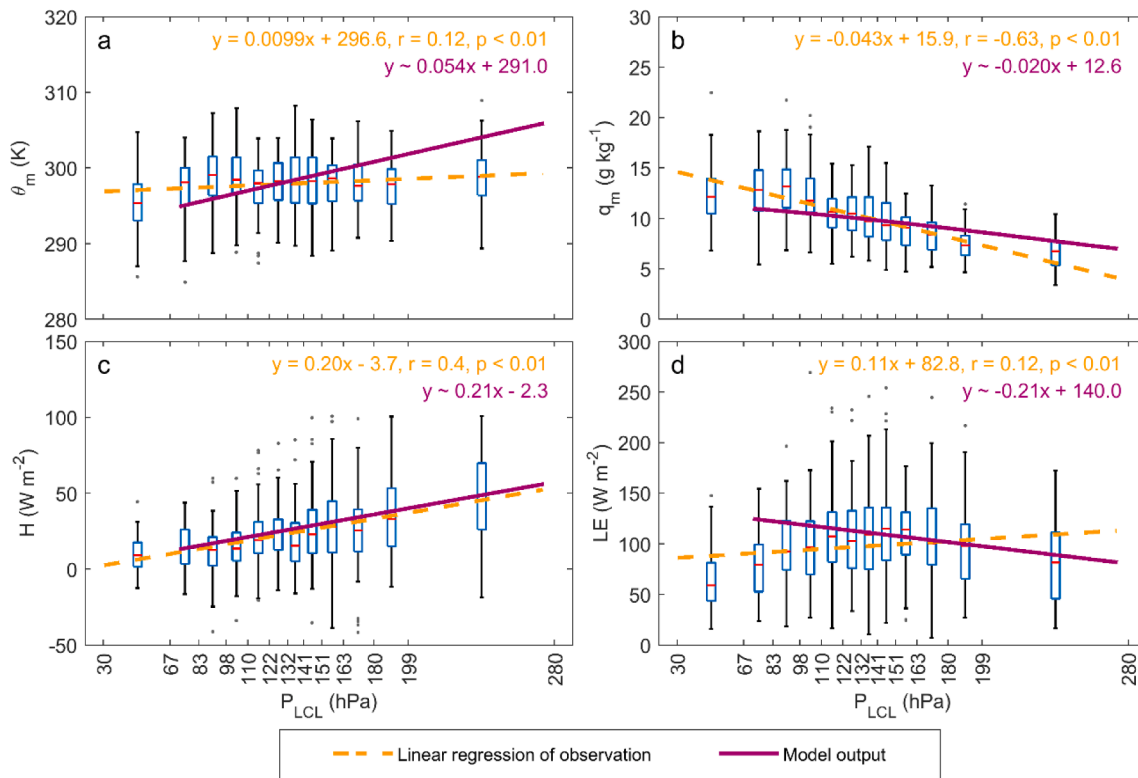
Fig. 2. Boxplots with bins containing equal numbers of observations and linear regressions of observations at US-Ro1 from June to August 2004–2012, compared with model outputs of mixed layer equilibrium solutions against pressure height of mixed layer (P_{LCL}): (a) potential temperature (θ_m); (b) specific humidity (q_m); (c) surface sensible heat flux (H); (d) surface latent heat flux (LE). The linear regressions were calculated from the daily average of observations (Fig. S1).

turn controls LE in the non-steady state (McColl and Rigden, 2020). The observations at US-Ro1 imply that the surface fluxes are consistent with SFE when the ML is well-developed. Although the entire set of observed LE is positively correlated to P_{LCL} (Fig. 2d), the observed LE is negatively correlated to P_{LCL} from 110 to 280 hPa ($LE = -0.25P_{LCL} + 142.9$, $r = -0.19$, $p < 0.01$), whose linear regression is closer to the model output. The large values of P_{LCL} are related to large values of r_c that correspond to a water-limited condition, which drives the surface fluxes toward the SFE condition.

The base model also shows good performance in surface energy partitioning with the constraint on observed Q and the assumption of complete energy balance closure. While the surface energy balance ratio (EBR $= (H + LE)/Q$) of Eq. (1) is assumed to be 100% in the model, the average EBR of the eddy covariance data at US-Ro1 for summer seasons from 2004 to 2012 is 86% (Table S1), which is within the typical range of eddy covariance measurements across FLUXNET sites (Stoy et al., 2013; Wilson et al., 2002). The sensitivity analysis on Q indicates that the evaporative fraction $LE/(H + LE)$ is well constrained by using the observed Q as the reference value in the base model (Fig. S3).

4.1.2. ML equilibrium of water isotope compositions

Fig. 3 shows that the model generates reasonable isotope ratios and deuterium excess values in the ML compared with the observations at US-Ro1 in summer 2010 to 2012. The observed δD_m and $\delta^{18}O_m$ both weakly decrease with P_{LCL} with slopes of -0.097 ‰ hPa^{-1} ($p = 0.03$) and -0.005‰ hPa^{-1} ($p = 0.49$), respectively (Fig. 3a). The model solutions of δD_m and $\delta^{18}O_m$ display the same negative trends with slopes of -0.033 ‰ hPa^{-1} and -0.018 ‰ hPa^{-1}, respectively (Fig. 3b) The modeled and observed d_m both increase with P_{LCL} with slopes of 0.038 ‰ hPa^{-1} ($p = 0.17$) and 0.11 ‰ hPa^{-1}, respectively (Fig. 3c). The modeled curves of δD_m, $\delta^{18}O_m$ and d_m all pass between, or approach, the 95% confidence bounds of the corresponding linear regressions of the observations. Therefore, although the isotope module calculated the mass mixing ratio

of H$_2$O, HDO and H$_2^{18}$O independently, the modeled values and trends of isotope ratios and deuterium excess are realistic when compared with the observations, demonstrating that the ML isotope equilibrium of each isotopologue is well-constrained by the model.

The sensitivity tests on the kinetic fractionation factors of evaporation (η_D and η_{18O}) indicate that these factors can significantly influence the relationship between isotope ratios and P_{LCL}. The kinetic fractionation during evaporation is caused by the differences in molecular diffusivities of isotopic species, and it is not a constant, as it is influenced by the near-surface atmospheric condition (Lee et al., 2009; Merlivat and Jouzel, 1979). The laboratory ranges of η_D and η_{18O} are 0.9796–0.9955 and 0.9724–0.9943, respectively (Horita et al., 2008). The sensitivity tests showed that δD_m is insensitive to η_D, so η_D takes the average lab value of 0.9892. The value of η_{18O} is determined as 0.9930 by best fitting the model outputs to the linear regression of observation and is consistent with the results of Lagrangian simulations of the isotope composition of evaporation in Europe (Pfahl and Wemli, 2009) and the estimates found for a soybean field calculated under low-wind condition (Lee et al., 2009).

4.1.3. Sensitivity to canopy resistance

Figs. 4 and S4 take two choices of canopy resistance ($r_c = 263$ and 460 s m^{-1}) with reference parameters to show the modeled equilibrium solutions of fluxes and variables. In the base model, when r_c increases from 263 to 460 s m^{-1}, H_0 increases and LE$_0$ declines, and the ML pressure height P_{LCL} increases from 150 to 200 hPa corresponding to the enhanced H_0 (Fig. S4). The radiative cooling term F_{rad} increases with P_{LCL} at a given radiative cooling rate $\partial\theta_{rad}/\partial t$. The thermal entrainment at the cloud base H_b increases to maintain the thermal equilibrium. The surface temperature T_0, potential temperatures θ_m and θ_{cld} also increase to the new equilibrium. As ET decreases, both the entrainment terms E_b and E_t decrease, and the specific humidities q_m and q_{cld} also decrease. Because the precipitation rate P and the rain evaporation fraction f are
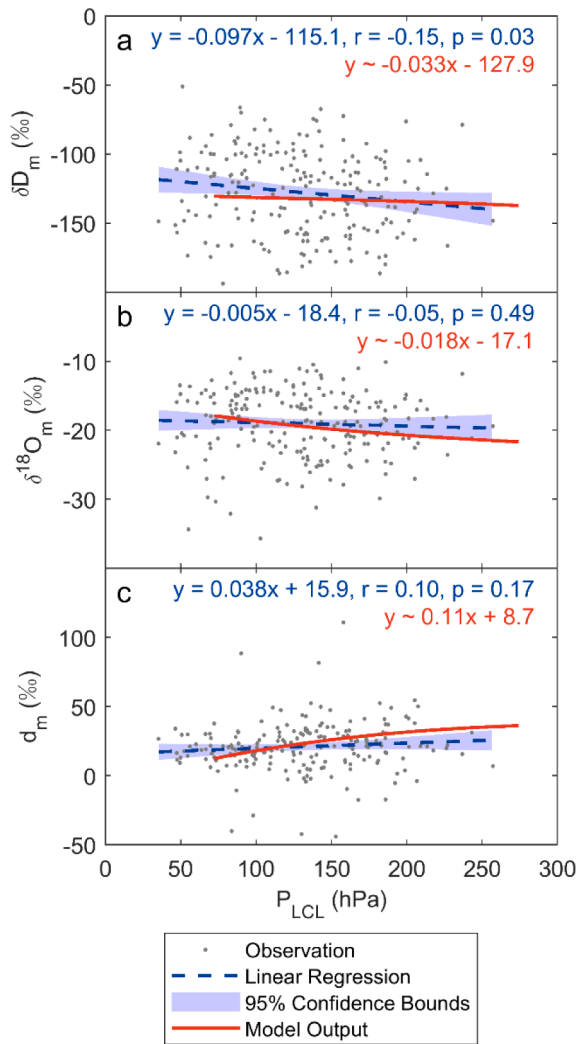
Fig. 3. Comparison of mixed layer equilibrium solutions and daily average isotope compositions at the tall tower in Rosemount, MN from June to August 2010–2012 against pressure height of mixed layer (P_{LCL}): (a) hydrogen isotope composition (δD_m); (b) oxygen isotope composition ($\delta^{18}O_m$); (c) deuterium excess $d_m = \delta D_m - 8\delta^{18}O_m$.

prescribed, the condensation $E_{C,L}$ and $E_{C,A}$, rain evaporation E_P, and precipitation cooling term F_{evap} remain unchanged.

In the water isotope module, all mass fluxes of HDO and $H_2^{18}O$ decrease with the moisture fluxes (i.e. mass fluxes of H_2O) (Fig. 4). The decline of isotope fluxes depletes the PBL and reduces the isotope ratios of ML (δD_m and $\delta^{18}O_m$). As T_0 increases, the liquid-vapor equilibrium fractionation factors of HDO (α_D) and $H_2^{18}O$ (α_{18O}) decrease at different rates, causing the deuterium isotope ratio of ET (δD_{E0}) to increase, while the oxygen isotope ratio of ET ($\delta^{18}O_{E0}$) decreases. The hydrogen and oxygen isotope ratios of entrainment at the cloud base (δD_{Eb} and $\delta^{18}O_{Eb}$) follow the same trend of δD_{E0} and $\delta^{18}O_{E0}$, respectively, to maintain the ML equilibrium. Due to the local water recycling, the isotope ratios of precipitation (δD_P and $\delta^{18}O_P$) also increase or decrease with δD_{E0} and $\delta^{18}O_{E0}$, respectively.

4.2. Sensitivity analyses of the water isotope module

In this section, the analyses focus on the sensitivities of the water isotope composition of ML water vapor (δD_m, $\delta^{18}O_m$) and precipitation (δD_P, $\delta^{18}O_P$) to precipitation parameters and boundary variables in the water isotope module. Tables 2 and 3 show the case studies examining the sensitivities of isotope fluxes and compositions to these parameters

or variables with r_c given as 263 s m^{-1} (i.e. P_{LCL} is 150 hPa in the reference case). Case (a) is the reference case, and Cases (b) to (f) are scenarios with varied P, f, LRR, free-atmosphere isotope compositions (δD_t and $\delta^{18}O_t$), and surface isotope compositions (δD_0 and $\delta^{18}O_0$), respectively.

4.2.1. Sensitivity to precipitation rate

Sensitivity tests show that when precipitation rate (P) increases by about 80% (from 3.3 to 6 mm day^{-1}), both hydrogen and oxygen isotope compositions of P and E_P get enriched by less than 1.5%, indicating that these isotope compositions are insensitive to P Tables 2b and 3b). Taking the assumption that the isotope composition of raindrops is in equilibrium with the surrounding air in the CBL (Eqs. (25) and ((26)), the isotope molar ratios of precipitation (R_P) and rain evaporation (R_{EP}) are calculated as:

$$R_P = \frac{P_i}{P}\frac{M_w}{M_i} = \frac{1-f/\alpha_e(T_{ML})}{1-f}\left[LRR\cdot\alpha(T_{CL})\frac{E_{i,0}}{E_0}+(1-LRR)\alpha(T_t)\frac{q_{i,t}}{q_t}\right]\frac{M_w}{M_i},$$
(29)

$$R_{E_P} = \frac{E_{i,P}}{E_P}\frac{M_w}{M_i} = \left[LRR\frac{\alpha(T_{CL})}{\alpha_e(T_{ML})}\frac{E_{i,0}}{E_0}+(1-LRR)\frac{\alpha(T_t)}{\alpha_e(T_{ML})}\frac{q_{i,t}}{q_t}\right]\frac{M_w}{M_i}.$$
(30)

These two equations show that P does not explicitly affect the isotope composition of either rainwater or rain evaporated vapor. Instead, P indirectly affects R_P and R_{EP} through the thermal and moisture variables, such as T_{ML} and T_{CL}, by changing E_P and F_{evap} in the base model.

4.2.2. Sensitivity to rain evaporation fraction

Tables 2c and 3c show that when rain evaporation fraction (f) increases, the isotope composition of all moisture fluxes increases, except for the surface ET. The isotope mass fluxes of ET are weakened in order to balance the increased mass fluxes of rain evaporation to reach the new ML equilibrium. The precipitation is more enriched in heavy isotopes responding to the stronger E_P, but the isotope ratios of E_P do not change significantly. Eqs. (29) and (30) show that R_P is explicitly determined by f while R_{EP} is not. R_P increases as f increases because light isotopes are more preferentially evaporated and leave the remaining water more enriched in heavy isotopes. R_{EP} represents the isotope mixing between the moisture of surface ET and the free atmosphere, and it is indirectly affected by f through the changes of thermal and moisture equilibrium in the base model.

Fig. 5a–c show that when f increases, the equilibrium isotope composition of water vapor in the ML decreases and the corresponding deuterium excess values increase. When f varies from 0 to 0.4, the ranges of modeled δD_m and $\delta^{18}O_m$ are -140.0 to -130.1‰ and -25.1 to -17.5‰, respectively. This explains 7% and 29% of the ranges of observed daily averaged δD_m (-193.7 to -51.2‰) and $\delta^{18}O_m$ (-35.7 to -9.6‰), respectively. The larger variation of modeled $\delta^{18}O_m$ indicates that the equilibrium $\delta^{18}O_m$ is more sensitive to f than δD_m. In contrast, when f increases, the rainwater gets more enriched in heavy isotopes and the corresponding deuterium excess values decrease (Fig. 5d–f). The observed deuterium excess of precipitation, d_P, is well bounded by curves modeled with f varying between 0 and 0.3. This indicates that the range of f can be constrained by d_P, and the upper bound for f in the Upper Midwest US is 0.3, which is smaller than the upper bound of 0.5 determined for tropical ecosystems (Worden et al., 2007). This implies that the lower air temperature and weaker convection in mid-latitude regions cause weaker rain evaporation compared to the tropical region.

Here we attempt to quantify f with P and rainwater isotope compositions (δD_P and $\delta^{18}O_P$) by relating them to the "amount effect", which is an empirical finding that the monthly mean isotope ratio of rainwater is anti-correlated to the precipitation amount in tropical regions (Dansgaard, 1964; Tharammal et al., 2017). Although the amount effect is most obvious in the tropics, it is also observed in the Midwestern US in summer seasons (Bedaso and Wu, 2020; Simpkins, 1995). There are multiple mechanisms that cause the amount effect, such as the
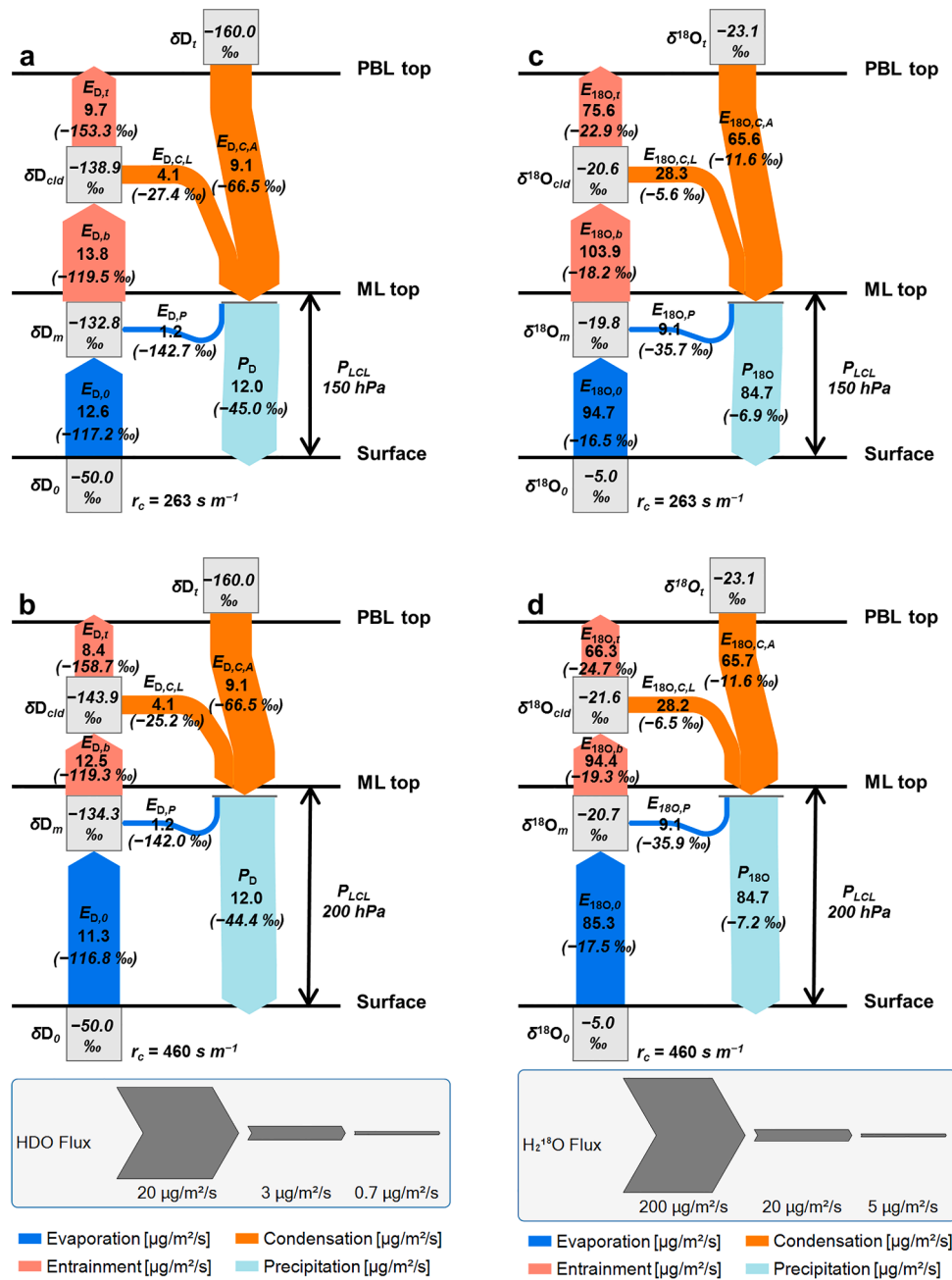
Fig. 4. Equilibrium solutions of the water isotope module at two different ML heights (P_{LCL}): equilibrium solutions of HDO fluxes at (a) P_{LCL} = 150 hPa and (b) P_{LCL} = 200 hPa; equilibrium solutions of H$_2^{18}$O fluxes at (c) P_{LCL} = 150 hPa and (d) P_{LCL} = 200 hPa. The numbers in parentheses indicate the isotope ratios of corresponding fluxes.

downdraft mixing of deep convection into the ML (Risi et al., 2008), mesoscale convective systems in stratiform rainfall (Kurita, 2013), and moisture convergence (Moore et al., 2014). Here we consider a classic explanation of the amount effect related to the rain evaporation. As the precipitation gets more intense, the raindrops are less equilibrated with the surrounding vapor because of higher ambient relative humidity, larger drops, and shorter residence time of raindrop formation, which causes a smaller fraction of rain evaporation and isotopic depletion of raindrops (Dansgaard, 1964; Lee and Fung, 2008; Risi et al., 2008). The typical ranges of amount effect in the tropical regions for $\partial \delta D_P / \partial P$ and $\partial \delta^{18}O_P / \partial P$ are -1 to $-8‰$ (mm day^{-1})$^{-1}$ and -0.5 to $-3‰$ (mm day^{-1})$^{-1}$, respectively (Eastoe and Dettman, 2016; Kurita, 2013; Risi et al., 2008; Tharammal et al., 2017). When P increases as shown in Tables 2b and 3b, the modeled $\partial \delta D_P / \partial P$ and $\partial \delta^{18}O_P / \partial P$ are 0.04 and

0.07‰ (mm day^{-1})$^{-1}$, respectively. Therefore, the model cannot simulate the amount effect when f is independent of P. To produce the amount effect, we made an arbitrary assumption that f is inversely proportional to P, i.e. $f = c_f / P$, where c_f is a prescribed parameter. A larger c_f indicates a stronger intensity of rain evaporation.

Fig. 5g–i show the sensitivity diagrams of rain evaporation fraction with c_f varying from 0 to 0.4 mm day^{-1}, on planes with the axes of isotope compositions of rainwater and summer mean precipitation rate. Using the observed summer mean precipitation rate at US-Ro1 and the amount-weighted isotope compositions of rainwater in 2006–2010, the diagrams with isotope ratios of rainwater (δD_P and $\delta^{18}O_P$) and deuterium excess value (d_P) consistently estimate that 0.3 mm day^{-1} is a reasonable value for c_f at US-Ro1. The corresponding f is estimated to be 0.09 with c_f = 0.3 mm day^{-1}. The magnitude of the amount effect can be

Table 2

Sensitivity results of mass fluxes and isotope ratios of the hydrogen isotope composition (HDO) corresponding to the model parameters.

Case	r_c	P	f	LRR	δD_t	δD_0	P_{LCL}
	(s m^{-1})	(mm day^{-1})	(-)	(-)	(‰)	(‰)	(hPa)
a	263	3.3	0.1	0.3	−160.0	−50.0	150
b	263	**6.0**	0.1	0.3	−160.0	−50.0	141
c	263	3.3	**0.2**	0.3	−160.0	−50.0	136
d	263	3.3	0.1	**0.5**	−160.0	−50.0	150
e	263	3.3	0.1	0.3	**−200.0**	−50.0	150
f	263	3.3	0.1	0.3	−160.0	**−40.0**	150

Case	$E_{D,o}$	$E_{D,b}$	$E_{D,t}$	$E_{D,C,L}$	$E_{D,C,A}$	$E_{D,P}$	P_D
	(µg m^{-2} s^{-1})	(µg m^{-2} s^{-1})	(µg m^{-2} s^{-1})	(µg m^{-2} s^{-1})	(µg m^{-2} s^{-1})	(µg m^{-2} s^{-1})	(µg m^{-2} s^{-1})
a	12.6	13.8	9.7	4.1	9.1	1.2	12.0
b	12.0	14.1	6.7	7.4	16.6	2.2	21.8
c	11.6	14.3	9.8	4.6	10.3	2.7	12.2
d	12.6	13.8	7.0	6.8	6.5	1.2	12.1
e	12.7	13.8	9.7	4.1	8.7	1.2	11.7
f	12.7	13.9	9.8	4.1	9.1	1.2	12.1

Case	δD_{E0}	δD_m	δD_{Eb}	δD_{cld}	δD_{Et}
	(‰)	(‰)	(‰)	(‰)	(‰)
a	−117.2	−132.8	−119.5	−138.9	−153.3
b	−116.5	−133.4	−120.6	−138.8	−204.8
c	−116.1	−133.7	−121.2	−138.8	−159.7
d	−117.4	−132.5	−119.0	−138.7	−193.2
e	−109.3	−142.7	−114.6	−155.6	−149.8
f	−106.1	−125.8	−109.1	−133.6	−143.6

Case	$\delta D_{EC,L}$	$\delta D_{EC,A}$	δD_{EC}	δD_{EP}	δD_P
	(‰)	(‰)	(‰)	(‰)	(‰)
a	−27.4	−66.5	−54.8	−142.7	−45.0
b	−27.0	−66.5	−54.7	−142.7	−44.9
c	−26.7	−66.5	−54.6	−142.7	−32.6
d	−27.7	−66.5	−47.1	−135.7	−37.3
e	−18.7	−111.0	−83.3	−168.6	−73.8
f	−15.2	−66.5	−51.2	−139.4	−41.3

quantified from the slope of the δ_P–P curve at a specific c_f. The modeled $\partial\delta D_P/\partial P$ is −2.8‰ (mm day^{-1})$^{-1}$ and $\partial\delta^{18}O_P/\partial P$ is −0.8‰ (mm day^{-1})$^{-1}$ at US-Ro1. These values are near the lower bound of the amount effect observed in the tropics, implying that the amount effect in the summer Upper Midwest region is weaker compared to the tropical average.

4.2.3. Sensitivity to local recycling ratio

The local recycling ratio (LRR) primarily affects the isotope mass fluxes and isotope compositions of E_t, P and E_P, while the isotope composition of ML water vapor is insensitive to LRR Tables 2d and 3d). Fig. 6 shows that the shapes of the sensitivity curves are bounded by the curves with LRR = 0 and LRR = 1. Eqs. (29) and ((30) indicate that LRR represents the two-source mixing ratio for R_P and R_{EP} between the moisture from surface ET and the advected moisture above the PBL. When LRR = 0, R_P and R_{EP} are purely determined by the moisture condition above the PBL (i.e. δD_t and $\delta^{18}O_t$); when LRR = 1, R_P and R_{EP} are solely determined by the surface condition (i.e. δD_0 and $\delta^{18}O_0$) affecting the ET. Therefore, the change of boundary conditions above the PBL and at the surface may affect the sensitivities of δD_P and $\delta^{18}O_P$ to LRR. The sensitivity tests on the boundary isotope compositions indicate that these boundary variables are well constrained (see Sections 4.2.4 and 4.2.5).

Fig. 6c and d show a graphical method to quantify LRR combining the information of surface ET and the isotope ratios of precipitation at the seasonal timescale. When ET is fixed, rainwater is more enriched in heavy isotopes as LRR increases. Due to different values of fractionation factors of HDO and H$_2^{18}$O, when ET increases at a given LRR, δD_P decreases and $\delta^{18}O_P$ increases. This is consistent with conditions that smaller deuterium excess values of precipitation indicate larger influences by ET through recycling (Xia and Winnick, 2021). By

comparing with the observation of summer mean ET at US-Ro1 and the amount-weighted isotope compositions of rainwater from 2006 to 2010, the diagrams of δD_P–ET and $\delta^{18}O_P$–ET estimate LRR as 0.28 and 0.33, respectively. To assess the uncertainty range of LRR due to the observation uncertainties in rainwater isotope composition, a Monte Carlo method was used to randomly resample 30 of the 85 rainfall events for 10^5 iterations. LRR was 0.26 ± 0.10 and 0.32 ± 0.13 (mean ± standard deviation), estimated with δD_P and $\delta^{18}O_P$, respectively. The ensemble estimate for LRR was 0.29 ± 0.12. Therefore, LRR = 0.3 appears to be well constrained for this study region, and is consistent with previous approaches for the region (Griffis et al., 2016). The mean summertime estimates of LRR derived from the δD_P–ET and $\delta^{18}O_P$–ET diagrams for the years 2006 to 2010 are 0.35, 0.36, 0.17, 0.29, and 0.29, respectively. The lowest LRR in 2008 coincided with the lowest precipitation and second lowest ET among the five years (Table S1). This suggests that a dry year impeded the crop growth and consequently decreased ET and LRR.

It is well known that LRR depends on the shape and area of the study region. The LRR value increases as a function of spatial scale (Brubaker et al., 2001; Burde and Zangvil, 2001; Dominguez et al., 2006; Van Der Ent and Savenije, 2011). The summer recycling ratio of the contiguous US varies between 0.1 and 0.3 given a scale area of 10^6 km^2 (Dominguez et al., 2006; Harding and Snyder, 2012; Zangvil et al., 2004). Considering a North American continental scale source region of ET, the summer recycling ratio can be up to 0.4–0.5 (Gimeno et al., 2012; Van Der Ent et al., 2010). The spatial scale of the equilibrium model is on the order of 150–450 km, assuming a daily average wind speed of 2–5 m/s in the lower atmosphere as suggested by B04. The monthly source footprints of the tall tower water vapor measurement covered a large portion of North American continent (Griffis et al., 2016), which is much larger than the equilibrium model spatial scale. Some estimated values of LRR

Table 3

Sensitivity results of mass fluxes and isotope ratios of the oxygen isotope composition ($H_2^{18}O$) corresponding to the model parameters.

Case	r_c (s m^{-1})	P (mm day^{-1})	f (-)	LRR (-)	$\delta^{18}O_t$ (‰)	$\delta^{18}O_0$ (‰)	P_{LCL} (hPa)
a	263	3.3	0.1	0.3	−23.1	−5.0	150
b	263	**6.0**	0.1	0.3	−23.1	−5.0	141
c	263	3.3	**0.2**	0.3	−23.1	−5.0	136
d	263	3.3	0.1	**0.5**	−23.1	−5.0	150
e	263	3.3	0.1	0.3	**−30.0**	−5.0	150
f	263	3.3	0.1	0.3	−23.1	**−2.5**	150

Case	$E_{18O,0}$ (μg m^{-2} s^{-1})	$E_{18O,b}$ (μg m^{-2} s^{-1})	$E_{18O,t}$ (μg m^{-2} s^{-1})	$E_{18O,C,L}$ (μg m^{-2} s^{-1})	$E_{18O,C,A}$ (μg m^{-2} s^{-1})	$E_{18O,P}$ (μg m^{-2} s^{-1})	P_{18O} (μg m^{-2} s^{-1})
a	94.7	103.9	75.6	28.3	65.6	9.1	84.7
b	90.3	106.8	55.5	51.3	118.9	16.6	153.6
c	87.9	108.4	76.6	31.8	73.8	20.6	85.0
d	94.7	103.9	56.8	47.1	46.8	9.1	84.8
e	94.9	104.0	75.7	28.3	65.1	9.1	84.3
f	95.0	104.2	75.8	28.4	65.6	9.1	84.8

Case	$\delta^{18}O_{E0}$ (‰)	$\delta^{18}O_m$ (‰)	$\delta^{18}O_{Eb}$ (‰)	$\delta^{18}O_{cld}$ (‰)	$\delta^{18}O_{Et}$ (‰)
a	−16.5	−19.8	−18.2	−20.6	−22.9
b	−15.9	−20.3	−19.0	−20.9	−31.5
c	−15.5	−20.5	−19.3	−21.0	−25.3
d	−16.5	−19.8	−18.2	−20.5	−28.3
e	−15.2	−21.5	−17.4	−23.4	−22.2
f	−13.6	−18.0	−15.5	−19.1	−20.2

Case	$\delta^{18}O_{EC,L}$ (‰)	$\delta^{18}O_{EC,A}$ (‰)	$\delta^{18}O_{EC}$ (‰)	$\delta^{18}O_{EP}$ (‰)	$\delta^{18}O_P$ (‰)
a	−5.6	−11.6	−9.8	−35.7	−6.9
b	−5.0	−11.6	−9.6	−35.5	−6.7
c	−4.6	−11.6	−9.5	−35.4	−3.0
d	−5.7	−11.6	−8.6	−34.6	−5.8
e	−4.2	−18.6	−14.3	−40.0	−11.4
f	−2.6	−11.6	−8.9	−34.8	−6.0

over 0.3 might be associated with the PBL advection and reflect the moisture originated from outside of the study domain.

Since the PBL advection is ignored in the model setup, here we try to explore the source of advected moisture by estimating the deuterium excess values of the PBL advection (d_{adv}). Deuterium excess values associated with precipitation, ET and advection have been used to quantify LRR in previous studies (e.g. Kong et al., 2013; Peng et al., 2005). The value of d_{adv} was calculated using a transformation of their equation:

$$d_{adv} = \frac{d_P - LRR \cdot d_{ET}}{1 - LRR}, \tag{31}$$

where d_P and d_{ET} are the deuterium excess values of precipitation and ET, respectively. Using the observed d_P, the modeled d_{ET}, and the mean LRR estimated by the sensitivity diagrams, the summer d_{adv} values from 2006 to 2010 are estimated to be 16.9‰, 2.4‰, 3.9‰, 0.53‰, and 7.1‰, respectively.

According to Eq. (31), d_{adv} is identical to d_P when there is no water recycling (LRR = 0). Further, the Rayleigh distillation and rainout history will not affect the water vapor deuterium excess, which suggests that d_{adv} will be a passive tracer carrying the oceanic signal without local water recycling (Wei and Lee, 2019). The typical summer deuterium excess value of water vapor from the ocean varies between 0 and 20‰ due to different environmental relative humidity, sea surface temperature, and wind speed of the evaporation source (Benetti et al., 2014; Bonne et al., 2019; Steen-Larsen et al., 2015, 2014; Uemura et al., 2008). The average mid-afternoon deuterium excess of transpiration from cropland was close to the xylem water value of −3.5‰ (Welp et al.,

2012), and thus the continental source of water vapor tends to decrease the value of d_{adv}. Therefore, the small values of d_{adv} in 2007, 2008 and 2009 suggest that the dominant source of the advection was continental, while the source of the advection in 2006 and 2010 was mainly oceanic.

Eq. (31) also shows that the values of d_{adv} and LRR are anti-correlated. A continental advection with a small value of d_{adv} suggests a strong effect of local water recycling. Therefore, without the effect of advection, the model assumes that the deuterium excess of upstream advection is identical to the local situation. The LRR value may be overestimated without the information of oceanic advection. However, further research is required to verify these potential influences caused by advection.

4.2.4. Sensitivity to isotope composition above the PBL

Tables 2e and 3e show that when isotope compositions of water vapor above the PBL (δD_t and $\delta^{18}O_t$) decrease, $E_{C,A}$, P and E_P become relatively depleted in the heavy isotopes. Further, the isotope mass fluxes of E_0, E_b and E_t increase and the corresponding isotope composition becomes enriched to compensate for the larger vertical isotope gradient induced by the depletion at the PBL top. When δD_t decreases by 25% (from −160 to −200‰), the modeled δD_m and δD_{cld} decrease by 7.5% and 12%, respectively (Table 2e). When $\delta^{18}O_t$ decreases by 30% (from −23.1 to −30‰), the modeled $\delta^{18}O_m$ and $\delta^{18}O_{cld}$ decrease by 8.6% and 14%, respectively (Table 3e). The larger sensitivity of the CBL isotope composition compared to the ML isotope composition illustrates that the depleted isotope signal is transported downward from the free atmosphere to the surface layer.

Fig. 7a and b show that when P_{LCL} is fixed, the modeled δD_m and δD_P decrease as δD_t declines. As P_{LCL} increases, their sensitivities to δD_t both increase. When P_{LCL} increases from 70 to 275 hPa, $\partial\delta D_m/\partial\delta D_t$ increases from 0.130 to 0.441, and $\partial\delta D_P/\partial\delta D_t$ increases from 0.69 to 0.75. Fig. 7c and d show that when P_{LCL} increases from 70 to 275 hPa, $\partial\delta^{18}O_m/\partial\delta^{18}O_t$ increases from 0.130 to 0.442, and $\partial\delta^{18}O_P/\partial\delta^{18}O_t$ increases from 0.62 to 0.68. The similar sensitivity of the oxygen and deuterium isotope composition indicates that the isotope depletion signal is transported by entrainment (Lee et al., 2012), which mixes different isotopologues at the same rate. The large sensitivities of $\partial\delta D_P/\partial\delta D_t$ and $\partial\delta^{18}O_P/\partial\delta^{18}O_t$ imply that the observed δD_P and $\delta^{18}O_P$ can effectively constrain δD_t and $\delta^{18}O_t$, respectively. The linear regressions of the observed δD_P and $\delta^{18}O_P$ against P_{LCL} suggest that the reference values of $\delta D_t = −160.0‰$ and $\delta^{18}O_t = −23.1‰$ are reasonable estimates for the upper boundary condition (Fig. 7b and d).

The sensitivity to the isotope composition of water vapor above the PBL may reveal the relative ratio of the continental effect between precipitation and the advected vapor above the PBL. The "continental effect" shows that the isotope ratios of precipitation and ambient vapor are gradually depleted from coastal to inland regions (Dansgaard, 1964; Winnick et al., 2014). The summer average gradient of the continental effect of rainwater $\partial\delta^{18}O_P/\partial x$ in the US is −4.8 ‰ (1000 km)$^{-1}$ (Liu et al., 2010; Welker, 2012; Winnick et al., 2014), and $\partial\delta D_P/\partial x$ is assumed to be −24 ‰ (1000 km)$^{-1}$ determined by the slope of the GMWL. The sensitivity test conducted here indicates that $\partial\delta D_P/\partial\delta D_t$ is about 0.7, and thus the continental effect of the hydrogen isotope composition of the free atmosphere $\partial\delta D_t/\partial x$ is estimated to be −34 ‰ (1000 km)$^{-1}$, which is a relatively good approximation of the gradient of the lower-atmosphere isotope composition from the US East Coast to the Upper Midwest region (Frankenberg et al., 2009; Sutanto et al., 2015). Since the continental effect is a composite phenomenon, caused by condensation from different oceanic sources and local water recycling of vapor from terrestrial ET (Welker, 2000; Winnick et al., 2014), future investigations are needed to partition the specific processes contributing to the relative ratio.

4.2.5. Sensitivity to isotope composition at the surface

When the isotope composition of soil water (δD_0 and $\delta^{18}O_0$) becomes relatively enriched in the heavy isotopes, the isotope mass fluxes and
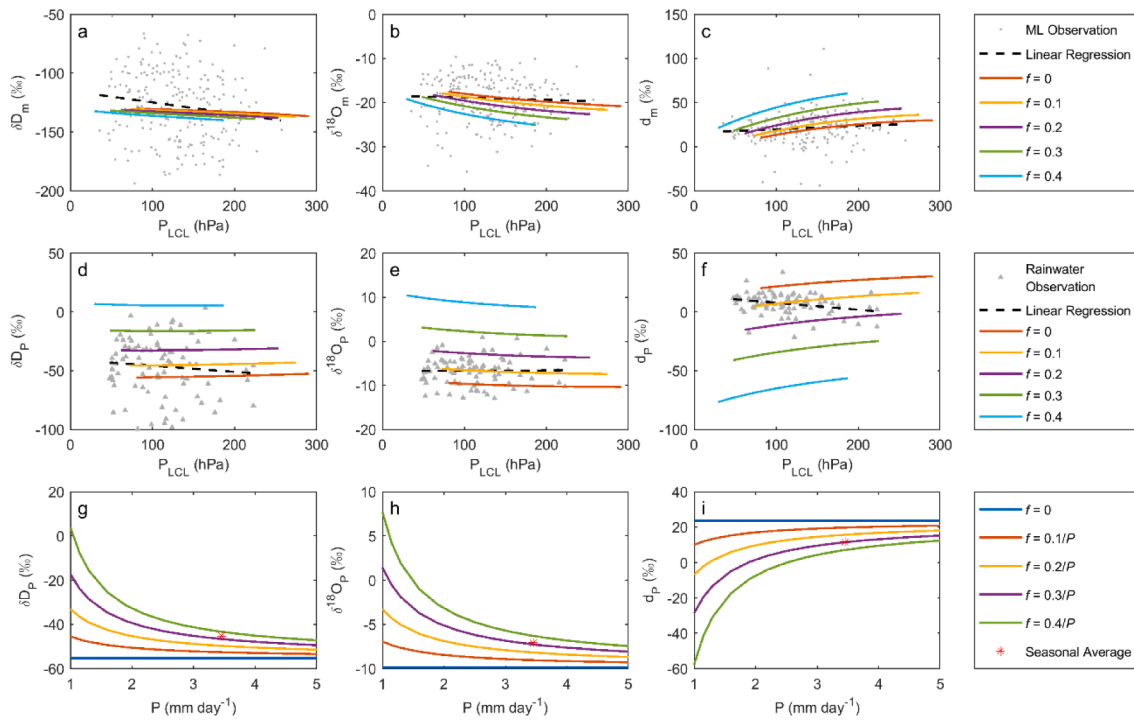
Fig. 5. Model solutions of sensitivity tests on rain evaporation fraction (f) compared with observations. Graphs in the first row are model outputs of water vapor isotope ratios in the ML compared with observations from the tall tower, Rosemount, MN in 2010–2012: (a) δD_m, (b) $\delta^{18}O_m$, and (c) deuterium excess $d_m = \delta D_m - \delta^{18}O_m$. Graphs in the second row are model outputs of rainwater isotope ratios compared with summer rainwater samples collected on the Saint Paul Campus, University of Minnesota in 2006–2010: (d) δD_P, (e) $\delta^{18}O_P$, and (f) $d_P = \delta D_P - \delta^{18}O_P$. Diagrams in the third row are the modeled isotope compositions of precipitation against varying seasonal precipitation rate (P) with the assumptions of f inversely proportional to P: (g) δD_P, (h) $\delta^{18}O_P$, and (i) $d_P = \delta D_P - \delta^{18}O_P$. The red asterisks in (g), (h) and (i) indicate the summer mean precipitation rate at US-Ro1 and amount-weighted isotope compositions of rainwater in 2006–2010.
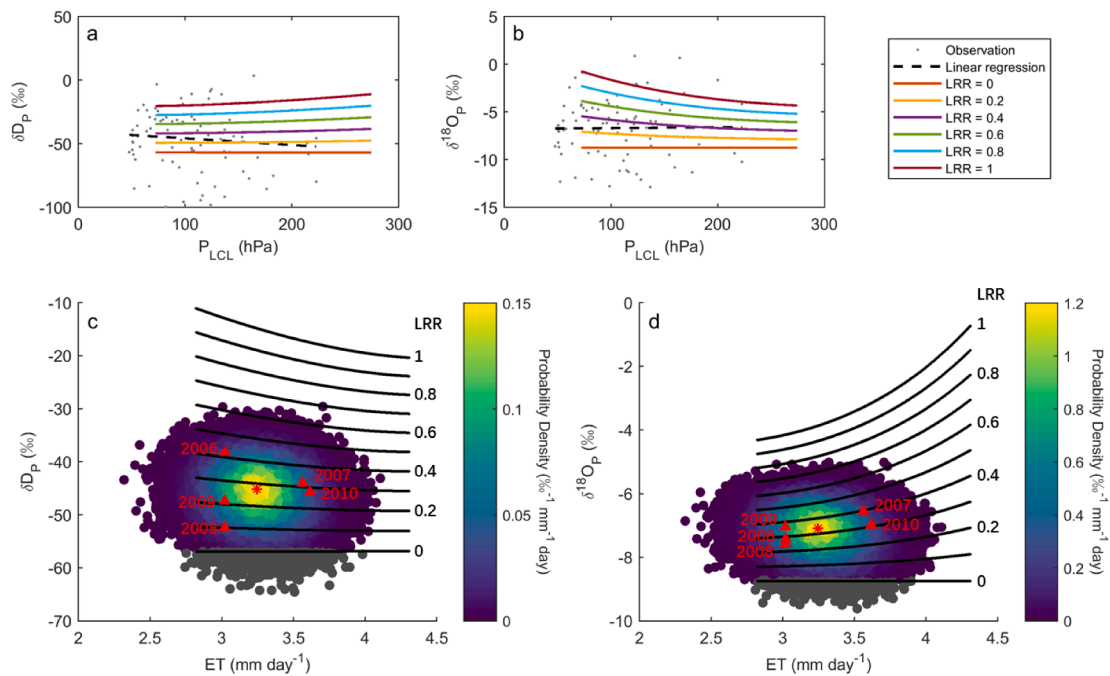
Fig. 6. Model solutions of sensitivity tests on local recycling ratio (LRR) compared with observations. Graphs in the first row are model outputs of rainwater isotope ratios compared with summer rainwater samples collected on the Saint Paul Campus, University of Minnesota in 2006–2010: (a) deuterium isotope ratio of precipitation (δD_P); and (b) oxygen isotope ratio of precipitation ($\delta^{18}O_P$). The second row are the sensitivity diagrams of LRR with modeled isotope compositions of precipitation against varying surface ET: (c) δD_P and (d) $\delta^{18}O_P$. In (c) and (d), the red asterisks indicate the summer mean ET at US-Ro1 and amount-weighted isotope compositions of rainwater in 2006–2010; the red triangles indicate the annual average of observations; and the colored circles indicate the resampled data generated in the Monte Carlo tests.
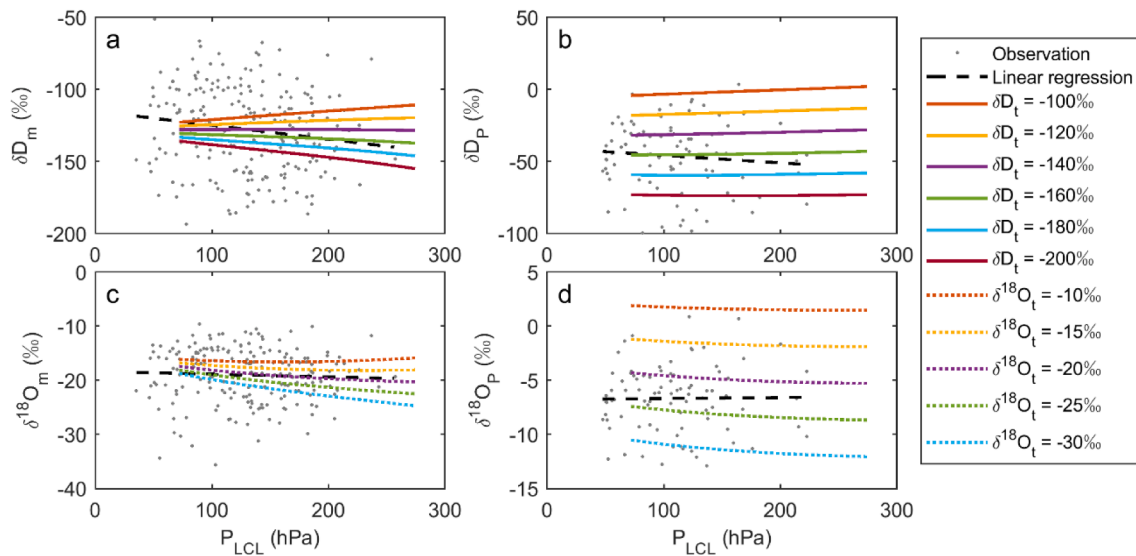
Fig. 7. Model solutions of sensitivity tests on isotope compositions above the PBL (δD_t and $\delta^{18}O_t$): hydrogen isotope composition of (a) water vapor in the ML and (b) rainwater; oxygen isotope composition of (c) water vapor in the ML and (d) rainwater.

isotope ratios of E_0, E_b, E_t and P increase (Tables 2f and 3f). When δD_0 increases by 20% (from -50 to -40‰), δD_m and δD_{cld} increase by 5.3% and 3.8%, respectively (Table 2f). When $\delta^{18}O_t$ increases by 50% (from -5 to -2.5‰), $\delta^{18}O_m$ and $\delta^{18}O_{cld}$ increase by 9.1% and 7.3%, respectively (Table 3f). The larger percentage increase in the isotope composition of the ML compared to the CBL confirms that the enriched surface isotope signal is transported upward.

The isotope composition of the ML and the precipitation both decrease when the surface becomes relatively depleted at a given ML height (Fig. 8). As the ML grows higher, the sensitivities of these isotope signals to the surface isotope composition decrease. When P_{LCL} increases from 70 to 275 hPa, $\partial \delta D_m / \partial \delta D_0$ and $\partial \delta^{18}O_m / \partial \delta^{18}O_0$ decreases from 0.80 to 0.52 and from 0.86 to 0.55, respectively (Fig. 8a and b). $\partial \delta D_P / \partial \delta D_0$ and $\partial \delta^{18}O_P / \partial \delta^{18}O_0$ increases slightly from 0.40 to 0.35 and from 0.39 to 0.33, respectively (Fig. 8c and d). The larger sensitivity of the ML isotope composition indicates that the surface isotope composition plays a major role in constraining the isotope equilibrium in the ML.

4.3. ET and local water recycling under different land surface scenarios

In this section, four types of land-cover surfaces, broadleaf forest (BLF), needleleaf forest (NLF), grassland (GRA) and cropland (CRO), were modeled and compared. The typical ranges of canopy resistance (r_c), transpiration fraction (T/ET), and leaf area index (LAI) of the four different ecosystems are presented in Fig. 9. The ranges of r_c were determined from a global estimate of canopy conductance (g_c, the reciprocal of r_c) derived from the MODIS remote sensing product (Yebra et al., 2013). The interval between median and 95% percentile of the Q75 value of the annual spatial mean was taken for the summer estimate in our study (Fig. 9a). The value of T/ET was modeled and computed by the isotope method for ET partitioning (Wang et al., 2010), and LAI was estimated from a global regression between T/ET and LAI (Wei et al., 2017) (see supplemental material Section S3.1).

The grassland has the highest range of r_c between 231 and 377 s m^{-1}, while the other three types largely overlap in the NLF range of 120–156 s m^{-1}, with BLF varying between 82 and 144 s m^{-1}, and CRO varying
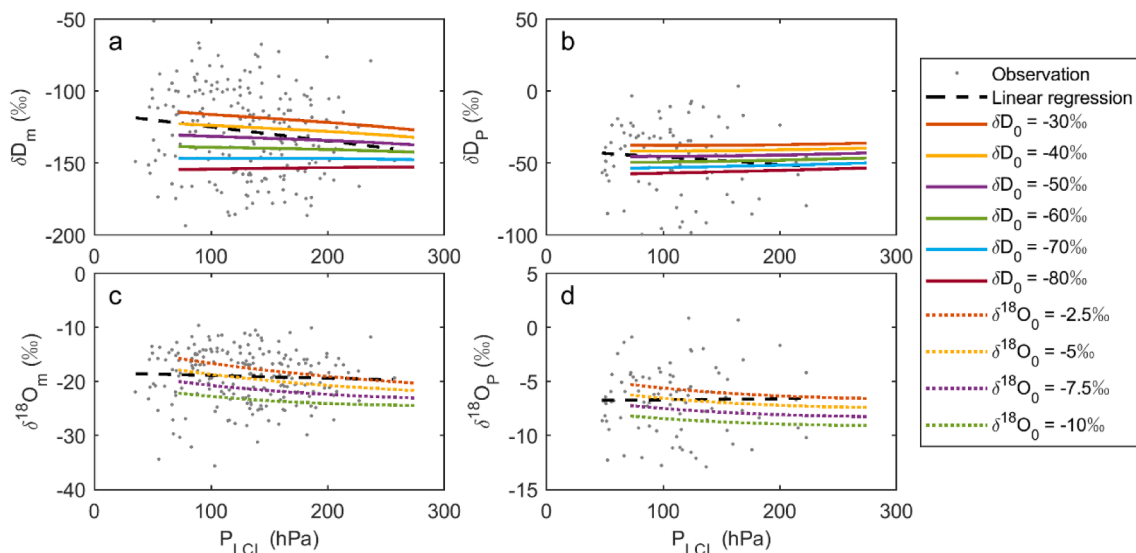
Fig. 8. Model solutions of sensitivity tests on isotope compositions at the surface (δD_0 and $\delta^{18}O_0$): hydrogen isotope composition of (a) water vapor in the ML and (b) rainwater; oxygen isotope composition of (c) water vapor in the ML and (d) rainwater.
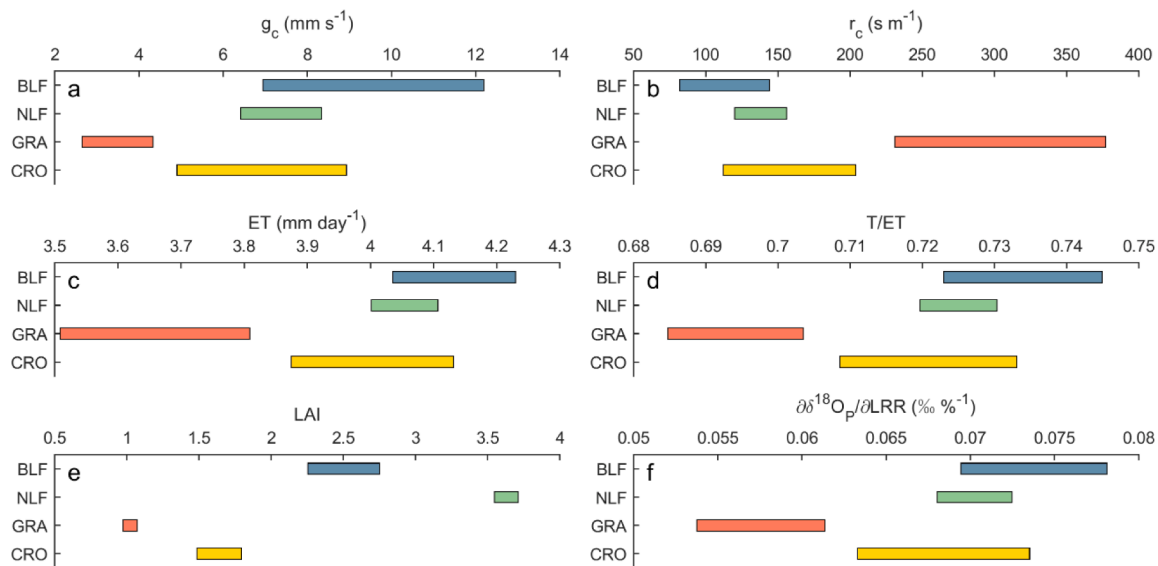
Fig. 9. Bars indicate the range of different variables under land cover scenarios of broadleaf forest (BLF), needleleaf forest (NLF), grassland (GRA) and cropland (CRO): (a) canopy conductance; (b) canopy resistance; (c) modeled total ET; (d) modeled transpiration fraction; (e) leaf area index (LAI); and (f) the partial derivative of oxygen isotope ratio of precipitation to the local recycling ratio (LRR).

from 112 to 204 s m^{-1} (Fig. 9b). Fig. 9c indicates that the ranking of the upper bound of modeled ET is BLF, CRO, NLF and GRA, which is consistent with the ranking of summer ET across AmeriFlux sites (Xia et al., 2015). Fig. 9d shows that the T/ET of the four land cover types ranges from 0.68 to 0.75, which are within the ranges of *in-situ* measurements in temperate ecosystems (Schlesinger and Jasechko, 2014). The idealized LAIs estimated from the T/ET relation for BLF, NLF, CRO and GRA are 2.3–2.8, 3.5–3.7, 1.5–1.8 and 1.0–1.1, respectively (Fig. 9e), which are smaller than the typical values of the corresponding ecosystems. The exponential regression of LAI is sensitive to T/ET (Eq. S10), and thus a small underestimate of T/ET might cause relatively large errors in LAI (Wei et al., 2017). Therefore, the values of LAI are presented here only as idealized quantities for showing the ranking and explaining the feedback processes of different ecosystems.

Fig. 10 shows different variables plotted with LAI as the x-axis. When LAI increases, r_c decreases nonlinearly (Fig. 10a) and causes the decline in P_{LCL} (Fig. 10b). The increase of LAI also induces a larger transpiration fraction (Fig. 10c) and causes enrichment in the oxygen isotope ratios of total ET ($\delta^{18}O_{E0}$) and soil evaporation ($\delta^{18}O_{Es}$) (Fig. 10d). When P_{LCL} gets smaller with a larger LAI, the ML is wetter, which reduces the term (1 − RH) in the denominator of the Craig–Gordon model (see supplemental material Section S3.1), and therefore the calculated soil evaporation vapor is more enriched in $H_2^{18}O$. Here $\delta^{18}O_{Es}$ was not validated by observations, and its uncertainty could influence the estimates of T/ET and LAI (Wei et al., 2015; Xiao et al., 2018).

The modeled $\delta^{18}O_{E0}$ of cropland ET ($\sim$ −15‰) is more depleted than the flux-weighted oxygen isotope composition of summer ET (−4.3‰) at US-Ro1 (Welp et al., 2008). The smaller $\delta^{18}O_{E0}$ could induce an underestimation of the modeled cropland T/ET. The calculated cropland T/ET is about 72%, while *in-situ* isotope partitioning in croplands suggests that transpiration can contribute over 80% to the total ET during the growing season (Xiao et al., 2018). The larger estimates in measurements might overestimate the daily average value because the isotope ET partitioning is usually applied with high transpiration in midday hours and soil evaporation is not accounted for when transpiration is weak (Wei et al., 2017). The other possible reason for the discrepancy might be the scale difference between the model and the stand-level measurements. Within the tall tower footprint of our study region (with a radius of about 100 km), the land cover percentages of cropland, grassland/pasture, broadleaf forest, and needleleaf forest are

48%, 11%, 12% and <1%, respectively (estimated from Cropland Data Layer, https://nassgeodata.gmu.edu/). The land use is remarkably similar as the radius increases to 400 km away from the tall tower, with land cover percentages of 44%, 11%, 15% and <1%, respectively, for the four land cover types. Therefore, the modeled $\delta^{18}O_{E0}$ might correspond to the climate average over a larger region with mixed land covers instead of homogeneous cropland.

The value of $\partial\delta^{18}O_P/\partial LRR$ quantifies the intensity of local water recycling affecting the oxygen isotope composition of rainwater at a fixed LAI or r_c. Fig. 9f shows that the median value of the cropland $\partial\delta^{18}O_P/\partial LRR$ is 1.19 times the grassland value and is 0.97 and 0.93 times the needle and broadleaf forest values, respectively. Therefore, the intensity of cropland is larger than grassland and comparable to forests. The change of $\partial\delta^{18}O_P/\partial LRR$ indicates the sensitivity of $\delta^{18}O_P$ affected by LAI through the local water recycling. The $\delta^{18}O_P$–ET diagram shows that $\delta^{18}O_P$ increases as ET increases at a given LRR (Fig. 6d). The increase of ET is caused by the increase of LAI (or decrease of r_c), which induces larger T/ET and more enrichment in oxygen isotope composition of ET ($\delta^{18}O_{E0}$) (Fig. 10d). As a result, the rainwater becomes more enriched in ^{18}O by the local water recycling with a larger LAI (and a smaller r_c). Therefore, when LAI increases (and r_c decreases), $\partial\delta^{18}O_P/\partial LRR$ becomes larger, indicating a stronger local water recycling effect on $\delta^{18}O_P$.

The land cover change to cropland could induce changes in local water recycling. Within the study region, grassland and broadleaf forest are two major natural vegetation types. If grassland is converted to cropland, the increase in LAI will cause a decline in the regional canopy resistance. Therefore, the total ET is expected to increase and the PBL height will decrease. The local water recycling will be intensified and cause an increase in $\delta^{18}O_P$. In contrast, the local water recycling will be weakened if broadleaf forest is converted to cropland. Assuming all cropland was originally grassland in the pre-agriculture era, the model estimates that the median LRR would have increased 19.5% in the modern time; and the median LRR would have decreased 7.6% compared with a pure broadleaf forest scenario.

The water management of croplands could also influence the local water recycling. Under drought conditions, the overall canopy resistance of the vegetative surface is expected to increase due to the increased water stress, and therefore it will decrease both ET and local recycling intensity. Broad-scale irrigation can counter these effects and increase local water recycling. Further, Alter et al. (2018) have
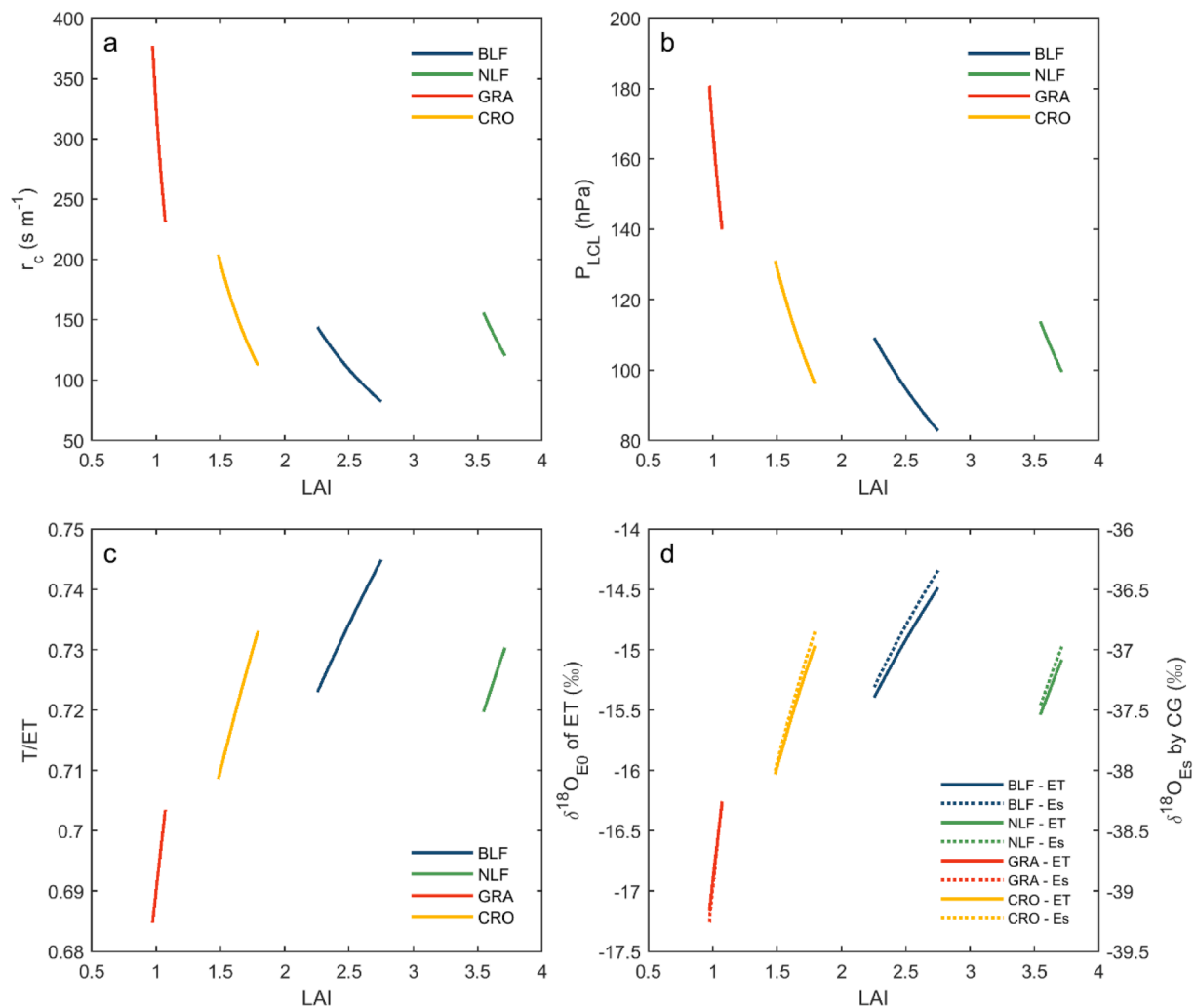
Fig. 10. Model outputs of different variables against leaf area index (LAI) under land cover scenarios of broadleaf forest (BLF), needleleaf forest (NLF), grassland (GRA) and cropland (CRO): (a) canopy resistance; (b) modeled pressure height of ML; (c) modeled transpiration fraction; and (d) the left y-axis and solid lines indicate the oxygen composition of ET represented by the modeled E_0, and the right y-axis and dotted lines indicate the oxygen composition of soil evaporation calculated by the Craig–Gordon (CG) model.

suggested that the increase of moist static energy near the surface and local water recycling are two major mechanisms through which the large-scale irrigation can contribute to enhanced rainfall recently observed in the central US. Here, the feedback process demonstrated by our equilibrium model further confirm that irrigation can enhance the local water recycling. Since the precipitation in the Upper Midwest US is predicted to be more variable under global warming scenarios (Zhang et al., 2021), irrigation use is expected to increase to offset variability in precipitation and to avoid more frequent drought events. Currently, about 3% of croplands are irrigated in the Upper Midwest US, and the annual total irrigation withdrawals about 1.48 billion tons of water in 2015 (Dieter et al., 2018). With the large coverage of cropland area and low percentage of irrigated ratio in the region, irrigation is expected to increase in the future and will likely enhance local water recycling.

4.4. Implications

The regional climate parameters (i.e. the rain evaporation fraction and local water recycling ratio) were quantified from flux and isotope observations using the model-generated sensitivity diagrams. According to the cooling effect and the influence on the isotope composition, the model results suggest that the rain evaporation is a key process in the ML equilibrium during the summer in the humid continental climate. The

model results for different vegetation scenarios implies that cropland in the Upper Midwest US has changed the intensity of local water recycling compared with the pre-agriculture era. The feedback processes in the model also reveal that the local water recycling is expected to be enhanced if irrigation is more frequently applied when considering future global warming scenarios. In future studies, the model can be coupled with other analytical land surface models to design more sophisticated water and agricultural management scenarios.

Global observations of stable water isotopes have identified multiple significant isotope effects in the global distribution, including the "amount effect", "continental effect", "temperature effect", and "latitude effect" (Dansgaard, 1964; Sutanto et al., 2015; Worden et al., 2007). Our model shows the potential capacity to simulate these isotope effects over monthly or longer timescales. For instance, by relating the rain evaporation fraction to the precipitation amount, the model can quantify the magnitude of the amount effect with the constraint of observed isotope composition of rainwater. The magnitude of the continental effect can be estimated by the model sensitivity between the isotope composition of rainwater and free-atmosphere water vapor. These results imply that the local water recycling is a key process influencing the continental effect.

Further research is needed to test the model performance across a broader range of ecosystems and environments. For example, the model

could be evaluated at other locations by utilizing the global isotope databases for precipitation and water vapor, such as the Global Network of Isotopes in Precipitation (GNIP) dataset and the Stable Water Vapor Isotope Database (SWVID) (Wei et al., 2019). In addition to the variables tested here (i.e. like the isotope ratios of rainwater and the ML water vapor), the isotope fluxes of ET, entrainment and condensation are potential quantities to further constrain the equilibrium model. B00 suggested that the equilibrium model is a plausible zero-order fit to the reanalysis data of a climate model. This implies that our model can be used to identify the patterns of isotope effects or the changes of water isotope equilibrium over the longer timescales. Such analytical analyses are simple but provide an important check on the more sophisticated isotope-enabled land-atmosphere models, which require more forcing data, more complex parameterization, and intensive computational resources.

5. Conclusion

(1) We developed an idealized water isotope model with precipitation processes and coupled it to a two-layer equilibrium boundary layer model. The model performed well in describing the summer PBL equilibrium of the hydrogen and oxygen isotope composition (HDO and $H_2^{18}O$) of water vapor and precipitation in the Upper Midwest, United States. The equilibrium values of these isotope isotopologues were well-constrained by the thermal and moisture equilibrium in the PBL.

(2) Two graphical methods were developed within the model framework to constrain the summer rain evaporation fraction and the local recycling ratio, respectively. For the Upper Midwest, United States region, we estimated the rain evaporation fraction to be 0.09 and local water recycling ratio to be 0.29 ± 0.12. The local water recycling ratios for the years 2006–2010 were 0.35, 0.36, 0.17, 0.29, and 0.29, respectively. The small recycling ratio in 2008 corresponded to a drought condition with the lowest precipitation and second lowest ET among the five years.

(3) Model sensitivity tests were used to quantify the isotope effects related to the amount effect and the continental effect. The summer magnitude of the amount effect for the study region is estimated as $-2.8‰$ $(\text{mm day}^{-1})^{-1}$ and $-0.8‰$ $(\text{mm day}^{-1})^{-1}$ for HDO and $H_2^{18}O$, respectively. The local water recycling is identified as a significant factor influencing the continental effect.

(4) The analyses of four land cover types (broadleaf forest, needleleaf forest, grassland, and cropland) and the feedback processes revealed by our model indicate that the local water recycling will decrease if broadleaf forest is converted to cropland, and it will increase if grassland is converted to cropland. The anthropogenic land use change in the Upper Midwest, United States has likely changed the local water recycling ratio by -7.6 to 19.5% under different land use change scenarios. The local water recycling is expected to be weakened under drought conditions, but it will be enhanced if irrigation is applied more intensely with more frequent drought events under global warming scenarios.

Declaration of Competing Interest

The authors declare that they have no known competing financial interests or personal relationships that could have appeared to influence the work reported in this paper.

Data availability

Data will be made available on request.

Supplementary materials

Supplementary material associated with this article can be found, in the online version, at doi:10.1016/j.agrformet.2023.109572.

References

Aggarwal, P.K., Romatschke, U., Araguas-Araguas, L., Belachew, D., Longstaffe, F.J., Berg, P., Schumacher, C., Funk, A., 2016. Proportions of convective and stratiform precipitation revealed in water isotope ratios. Nat. Geosci. 9, 624–629. https://doi.org/10.1038/ngeo2739.

Alter, R.E., Douglas, H.C., Winter, J.M., Eltahir, E.A.B., 2018. Twentieth century regional climate change during the summer in the Central United States attributed to agricultural intensification. Geophys. Res. Lett. 45, 1586–1594. https://doi.org/10.1002/2017GL075604.

Baker, J.M., Griffis, T.J., 2005. Examining strategies to improve the carbon balance of corn/soybean agriculture using Eddy covariance and mass balance techniques. Agric. For. Meteorol. 128, 163–177. https://doi.org/10.1016/j.agrformet.2004.11.005.

Bedaso, Z., Wu, S.Y., 2020. Daily precipitation isotope variation in Midwestern United States: implication for hydroclimate and moisture source. Sci. Total Environ. 713, 136631 https://doi.org/10.1016/j.scitotenv.2020.136631.

Beer, R., Glavich, T.A., Rider, D.M., 2001. Tropospheric emission spectrometer for the Earth Observing System's Aura satellite. Appl. Opt. 40, 2356. https://doi.org/10.1364/ao.40.002356.

Benetti, M., Reverdin, G., Pierre, C., Merlivat, L., Risi, C., Steen-larsen, H.C., Vimeux, F., 2014. Deuterium excess in marine water vapor: dependency on relative humidity and surface wind speed during evaporation 584–593. https://doi.org/10.1002/2013JD020535.Received.

Betts, A.K., 2000. Idealized model for equilibrium boundary layer over land. J. Hydrometeorol. 1, 507–523. https://doi.org/10.1175/1525-7541(2000)001<0507:IMFEBL>2.0.CO;2.

Betts, A.K., 1997. The Parameterization of Deep convection, in: The Physics and Parameterization of Moist Atmospheric Convection. Springer, Dordrecht, pp. 255–279. https://doi.org/10.1007/978-94-015-8828-7_10.

Betts, A.K., Helliker, B., Berry, J., 2004. Coupling between CO_2, water vapor, temperature, and radon and their fluxes in an idealized equilibrium boundary layer over land. J. Geophys. Res. Atmos. 109, 1–20. https://doi.org/10.1029/2003JD004420.

Bonne, J.L., Behrens, M., Meyer, H., Kipfstuhl, S., Rabe, B., Schönicke, L., Steen-Larsen, H.C., Werner, M., 2019. Resolving the controls of water vapour isotopes in the Atlantic sector. Nat. Commun. 10, 1–10. https://doi.org/10.1038/s41467-019-09242-6.

Bony, S., Risi, C., Vimeux, F., 2008. Influence of convective processes on the isotopic composition ($\delta^{18}O$ and δD) of precipitation and water vapor in the tropics: 1. Radiative-convective equilibrium and Tropical Ocean-Global Atmosphere-Coupled Ocean-Atmosphere Response Experiment. J. Geophys. Res. Atmos. 113, 1–21. https://doi.org/10.1029/2008JD009942.

Brubaker, K.L., Dirmeyer, P.A., Sudradjat, A., Levy, B.S., Bernal, F., 2001. A 36-yr climatological description of the evaporative sources of warm-season precipitation in the Mississippi River Basin. J. Hydrometeorol. 2, 537–557. https://doi.org/10.1175/1525-7541(2001)002<0537:AYCDOT>2.0.CO;2.

Burde, G.I., Zangvil, A., 2001. The estimation of regional precipitation recycling. Part II: a new recycling model. J. Clim. 14, 2509–2527. https://doi.org/10.1175/1520-0442(2001)014<2509:TEORPR>2.0.CO;2.

Cappa, C.D., Hendricks, M.B., DePaolo, D.J., Cohen, R.C., 2003. Isotopic fractionation of water during evaporation. J. Geophys. Res. Atmos. 108 https://doi.org/10.1029/2003jd003597.

Craig, H., 1961. Isotopic Variations in Meteoric Waters 133, 1702–1703. https://doi.org/10.1126/science.133.3465.1702.

Craig, H., Gordon, L.I., 1965. Deuterium and Oxygen 18 Variations in the Ocean and the Marine Atmosphere. Consiglio nazionale delle richerche, Laboratorio de geologia nucleare, Pisa.

Dansgaard, W., 1964. Stable isotopes in precipitation. Tellus 16, 436–468. https://doi.org/10.3402/tellusa.v16i4.8993.

Dieter, C.A., Maupin, M.A., Caldwell, R.R., Harris, M.A., Ivahnenko, T.I., Lovelace, J.K., Barber, N.L., Linsey, K.S., 2018. Estimated Use of Water in the United States in 2015: U.S. Geological Survey Circular 1441. USGS Publications Warehouse, Reston, VA. https://doi.org/10.3133/cir1441.

Dominguez, F., Kumar, P., Liang, X.Z., Ting, M., 2006. Impact of atmospheric moisture storage on precipitation recycling. J. Clim. 19, 1513–1530. https://doi.org/10.1175/JCLI3691.1.

Durack, P.J., Wijffels, S.E., Matear, R.J., 2012. Ocean salinities reveal strong global water cycle intensification during 1950 to 2000. Science 336, 455–458. https://doi.org/10.1126/science.1212222.

Eastoe, C.J., Dettman, D.L., 2016. Isotope amount effects in hydrologic and climate reconstructions of monsoon climates: implications of some long-term data sets for precipitation. Chem. Geol. 430, 78–89. https://doi.org/10.1016/j.chemgeo.2016.03.022.

Frankenberg, C., Yoshimura, K., Warneke, T., Aben, I., Butz, A., Deutscher, N., Griffith, D., Hase, F., Notholt, J., Schneider, M., Schrijver, H., Röckmann, T., 2009. Dynamic processes governing lower-tropospheric HDO/H$_2$O ratios as observed from space and ground. Science 325, 1374–1377. https://doi.org/10.1126/science.1173791.

Fu, Y., Qin, F., 2014. Summer daytime precipitation in ice, mixed and water phase as viewed by PR and VIRS in tropics and subtropics. Remote Sens. Atmosph. Cloud. Precipit. V, 925906. https://doi.org/10.1117/12.2069128.

Gimeno, L., Stohl, A., Trigo, R.M., Dominguez, F., Yoshimura, K., Yu, L., Drumond, A., Durn-Quesada, A.M., Nieto, R., 2012. Oceanic and terrestrial sources of continental precipitation. Rev. Geophys. 50, 1–41. https://doi.org/10.1029/2012RG000389.

Griffis, T.J., Lee, X., Baker, J.M., Billmark, K., Schultz, N., Erickson, M., Zhang, X., Fassbinder, J., Xiao, W., Hu, N., 2011. Oxygen isotope composition of evapotranspiration and its relation to C 4 photosynthetic discrimination. J. Geophys. Res. Biogeosci. 116, 1–21. https://doi.org/10.1029/2010JG001514.

Griffis, T.J., Sargent, S.D., Lee, X., Baker, J.M., Greene, J., Erickson, M., Zhang, X., Billmark, K., Schultz, N., Xiao, W., Hu, N., 2010. Determining the oxygen isotope composition of evapotranspiration using Eddy covariance. Bound.-Layer Meteorol. 137, 307–326. https://doi.org/10.1007/s10546-010-9529-5.

Griffis, T.J., Wood, J.D., Baker, J.M., Lee, X., Xiao, K., Chen, Z., Welp, L.R., Schultz, N.M., Gorski, G., Chen, M., Nieber, J., 2016. Investigating the source, transport, and isotope composition of water vapor in the planetary boundary layer. Atmos. Chem. Phys. 16, 5139–5157. https://doi.org/10.5194/acp-16-5139-2016.

Haghighi, E., Kirchner, J.W., 2017. Near-surface turbulence as a missing link in modeling evapotranspiration-soil moisture relationships. Water Resour. Res. 53, 5320–5344. https://doi.org/10.1002/2016WR020111.

Harding, K.J., Snyder, P.K., 2012. Modeling the atmospheric response to irrigation in the great plains. Part II: the precipitation of irrigated water and changes in precipitation recycling. J. Hydrometeorol. 13, 1687–1703. https://doi.org/10.1175/JHM-D-11-099.1.

He, H., Smith, R.B., 1999. Stable isotope composition of water vapor in the atmospheric boundary layer above the forests of New England. J. Geophys. Res. Atmos. 104, 11657–11673. https://doi.org/10.1029/1999JD900080.

Horita, J., Rozanski, K., Cohen, S., 2008. Isotope effects in the evaporation of water: a status report of the Craig-Gordon model. Isotope. Environ. Health Stud. 44, 23–49. https://doi.org/10.1080/10256010801887174.

Horita, J., Wesolowski, D.J., 1994. Liquid-vapor fractionation of oxygen and hydrogen isotopes of water from the freezing to the critical temperature. Geochim. Cosmochim. Acta 58, 3425–3437. https://doi.org/10.1016/0016-7037(94)90096-5.

Huntington, T.G., 2006. Evidence for intensification of the global water cycle: review and synthesis. J. Hydrol. 319, 83–95. https://doi.org/10.1016/j.jhydrol.2005.07.003.

Keys, P.W., Porkka, M., Wang-Erlandsson, L., Fetzer, I., Gleeson, T., Gordon, L.J., 2019. Invisible water security: moisture recycling and water resilience. Water Secur. 8, 100046 https://doi.org/10.1016/j.wasec.2019.100046.

Kong, Y., Pang, Z., Froehlich, K., 2013. Quantifying recycled moisture fraction in precipitation of an arid region using deuterium excess. Tellus, Ser. B Chem. Phys. Meteorol. 65 https://doi.org/10.3402/tellusb.v65i0.19251.

Kurita, N., 2013. Water isotopic variability in response to mesoscale convective system over the tropical ocean. J. Geophys. Res. Atmos. 118 https://doi.org/10.1002/jgrd.50754, 10,376–10,390.

Lai, C.T., Ehleringer, J.R., 2011. Deuterium excess reveals diurnal sources of water vapor in forest air. Oecologia 165, 213–223. https://doi.org/10.1007/s00442-010-1721-2.

Lee, J.E., Fung, I., 2008. Amount effect" of water isotopes and quantitative analysis of post-condensation processes. Hydrol. Process. 22, 1–8. https://doi.org/10.1002/hyp.6637.

Lee, X., Griffis, T.J., Baker, J.M., Billmark, K.A., Kim, K., Welp, L.R., 2009. Canopy-scale kinetic fractionation of atmospheric carbon dioxide and water vapor isotopes. Glob. Biogeochem. Cycles 23, 1–15. https://doi.org/10.1029/2008GB003331.

Lee, X., Huang, J., Patton, E.G., 2012. A large-Eddy simulation study of water vapour and carbon dioxide isotopes in the atmospheric boundary layer. Bound.-Layer Meteorol. 145, 229–248. https://doi.org/10.1007/s10546-011-9631-3.

Lee, X., Sargent, S., Smith, R., Tanner, B., 2005. In situ measurement of the water vapor ^{18}O/^{16}O isotope ratio for atmospheric and ecological applications. J. Atmos. Ocean. Technol. 22, 555–565. https://doi.org/10.1175/JTECH1719.1.

Liu, Z., Bowen, G.J., Welker, J.M., 2010. Atmospheric circulation is reflected in precipitation isotope gradients over the conterminous United States. J. Geophys. Res. Atmos. 115, 1–14. https://doi.org/10.1029/2010JD014175.

McColl, K.A., Rigden, A.J., 2020. Emergent simplicity of continental evapotranspiration. Geophys. Res. Lett. 47, 1–11. https://doi.org/10.1029/2020GL087101.

McColl, K.A., Salvucci, G.D., Gentine, P., 2019. Surface flux equilibrium theory explains an empirical estimate of water-limited daily evapotranspiration. J. Adv. Model. Earth Syst. 11, 2036–2049. https://doi.org/10.1029/2019MS001685.

McVicar, T.R., Roderick, M.L., Donohue, R.J., Li, L.T., Van Niel, T.G., Thomas, A., Grieser, J., Jhajharia, D., Himri, Y., Mahowald, N.M., Mescherskaya, A.V., Kruger, A. C., Rehman, S., Dinpashoh, Y., 2012. Global review and synthesis of trends in observed terrestrial near-surface wind speeds: implications for evaporation. J. Hydrol. 416–417, 182–205. https://doi.org/10.1016/j.jhydrol.2011.10.024.

Merlivat, L., Jouzel, J., 1979. Global climatic interpretation of the deuterium-oxygen 16 relationship for precipitation. J. Geophys. Res. 84, 5029–5033. https://doi.org/10.1029/JC084iC08p05029.

Moore, M., Kuang, Z., Blossey, P.N., 2014. A moisture budget perspective of the amount effect. Geophys. Res. Lett. 41, 1329–1335. https://doi.org/10.1002/2013GL058302.

Mülmenstädt, J., Sourdeval, O., Delanoë, J., Quaas, J., 2015. Frequency of occurrence of rain from liquid-, mixed-, and ice-phase clouds derived from A-Train satellite retrievals. Geophys. Res. Lett. 42, 6502–6509. https://doi.org/10.1002/2015GL064604.

Oki, T., Kanae, S., 2006. Global hydrological cycles and world water resources. Science 313, 1068–1072. https://doi.org/10.1126/science.1128845.

Peng, H., Mayer, B., Norman, A.-L., Krouse, H.R., 2005. Modelling of hydrogen and oxygen isotope compositions for local precipitation. Tellus B Chem. Phys. Meteorol. 57, 273–282. https://doi.org/10.3402/tellusb.v57i4.16545.

Pfahl, S., Wernli, H., 2009. Lagrangian simulations of stable isotopes in water vapor: an evaluation of nonequilibrium fractionation in the Craig-Gordon model. J. Geophys. Res. Atmos. 114, 1–12. https://doi.org/10.1029/2009JD012054.

Raupach, M.R., 2000. Equilibrium evaporation and the convective boundary layer. Bound.-Layer Meteorol 96, 107–142. https://doi.org/10.1023/a:1002675729075.

Risi, C., Bony, S., Vimeux, F., 2008. Influence of convective processes on the isotopic composition (δ^{18}O and δD) of precipitation and water vapor in the tropics: 2. Physical interpretation of the amount effect. J. Geophys. Res. Atmos. 113, 1–12. https://doi.org/10.1029/2008JD009943.

Santer, B.D., Mears, C., Wentz, F.J., Taylor, K.E., Gleckler, P.J., Wigley, T.M.L., Barnett, T.P., Boyle, J.S., Brüggemann, W., Gillette, N.P., Klein, S.A., Meehl, G.A., Nozawa, T., Pierce, D.W., Stott, P.A., Washington, W.M., Wehner, M.F., 2007. Identification of human-induced changes in atmospheric moisture content. Proc. Natl. Acad. Sci. U. S. A. 104, 15248–15253. https://doi.org/10.1073/pnas.0702872104.

Schlesinger, W.H., Jasechko, S., 2014. Transpiration in the global water cycle. Agric. For. Meteorol. 189–190, 115–117. https://doi.org/10.1016/j.agrformet.2014.01.011.

Schultz, N.M., Griffis, T.J., Lee, X., Baker, J.M., 2011. Identification and correction of spectral contamination in ^{2}H/^{1}H and ^{18}O/^{16}O measured in leaf, stem, and soil water. Rapid Commun. Mass Spectrom. 25, 3360–3368. https://doi.org/10.1002/rcm.5236.

Simpkins, W.W., 1995. Isotopic composition of precipitation in central Iowa. J. Hydrol. 172, 185–207. https://doi.org/10.1016/0022-1694(95)02694-K.

Steen-Larsen, H.C., Sveinbjörnsdottir, A.E., Jonsson, T., Ritter, F., Bonne, J.L., Masson-Delmotte, V., Sodemann, H., Blunier, T., Dahl-Jensen, D., Vinther, B.M., 2015. Moisture sources and synoptic to seasonal variability of North Atlantic water vapor isotopic composition. J. Geophys. Res. https://doi.org/10.1002/2015JD023234.

Steen-Larsen, H.C., Sveinbjörnsdottir, A.E., Peters, A.J., Masson-Delmotte, V., Guishard, M.P., Hsiao, G., Jouzel, J., Noone, D., Warren, J.K., White, J.W.C., 2014. Climatic controls on water vapor deuterium excess in the marine boundary layer of the North Atlantic based on 500 days of in situ, continuous measurements. Atmos. Chem. Phys. 14, 7741–7756. https://doi.org/10.5194/acp-14-7741-2014.

Stewart, M.K., 1975. Stable isotope fractionation due to evaporation and isotopic exchange of falling waterdrops: applications to atmospheric processes and evaporation of lakes. J. Geophys. Res. 80, 1133–1146. https://doi.org/10.1029/jc080i009p01133.

Stoy, P.C., Mauder, M., Foken, T., Marcolla, B., Boegh, E., Ibrom, A., Arain, M.A., Arneth, A., Aurela, M., Bernhofer, C., Cescatti, A., Dellwik, E., Duce, P., Gianelle, D., van Gorsel, E., Kiely, G., Knohl, A., Margolis, H., Mccaughey, H., Merbold, L., Montagnani, L., Papale, D., Reichstein, M., Saunders, M., Serrano-Ortiz, P., Sottocornola, M., Spano, D., Vaccari, F., Varlagin, A., 2013. A data-driven analysis of energy balance closure across FLUXNET research sites: the role of landscape scale heterogeneity. Agric. For. Meteorol. 171–172, 137–152. https://doi.org/10.1016/j.agrformet.2012.11.004.

Sutanto, S.J., Hoffmann, G., Scheepmaker, R.A., Worden, J., Houweling, S., Yoshimura, K., Aben, I., Röckmann, T., 2015. Global-scale remote sensing of water isotopologues in the troposphere: representation of first-order isotope effects. Atmos. Meas. Tech. 8, 999–1019. https://doi.org/10.5194/amt-8-999-2015.

te Wierik, S.A., Cammeraat, E.L.H., Gupta, J., Artzy-Randrup, Y.A., 2021. Reviewing the Impact of Land Use and Land-Use Change on Moisture Recycling and Precipitation Patterns. Water Resour. Res. 57 https://doi.org/10.1029/2020WR029234.

Tharammal, T., Bala, G., Noone, D., 2017. Impact of deep convection on the isotopic amount effect in tropical precipitation. J. Geophys. Res. 122, 1505–1523. https://doi.org/10.1002/2016JD025555.

Trenberth, K.E., 1999. Atmospheric moisture recycling: role of advection and local evaporation. J. Clim. 12, 1368–1381. https://doi.org/10.1175/1520-0442(1999)012<1368:amrroa>2.0.co;2.

Uemura, R., Matsui, Y., Yoshimura, K., Motoyama, H., Yoshida, N., 2008. Evidence of deuterium excess in water vapor as an indicator of ocean surface conditions. J. Geophys. Res. Atmos. 113, 1–10. https://doi.org/10.1029/2008JD010209.

Van Der Ent, R.J., Savenije, H.H.G., 2011. Length and time scales of atmospheric moisture recycling. Atmos. Chem. Phys. 11, 1853–1863. https://doi.org/10.5194/acp-11-1853-2011.

Van Der Ent, R.J., Savenije, H.H.G., Schaefli, B., Steele-Dunne, S.C., 2010. Origin and fate of atmospheric moisture over continents. Water Resour. Res. 46, 1–12. https://doi.org/10.1029/2010WR009127.

Van Der Ent, R.J., Wang-Erlandsson, L., Keys, P.W., Savenije, H.H.G., 2014. Contrasting roles of interception and transpiration in the hydrological cycle - Part 2: moisture recycling. Earth Syst. Dyn. 5, 471–489. https://doi.org/10.5194/esd-5-471-2014.

Wang, K., Dickinson, R.E., 2012. A review of global terrestrial evapotranspiration: observation, modeling, climatology, and climatic variability. Rev. Geophys. 50 https://doi.org/10.1029/2011RG000373.

Wang, L., Caylor, K.K., Villegas, J.C., Barron-Gafford, G.A., Breshears, D.D., Huxman, T.E., 2010. Partitioning evapotranspiration across gradients of woody plant cover: assessment of a stable isotope technique. Geophys. Res. Lett. 37, 1–7. https://doi.org/10.1029/2010GL043228.

Wei, Z., Lee, X., 2019. The utility of near-surface water vapor deuterium excess as an indicator of atmospheric moisture source. J. Hydrol. 577, 123923 https://doi.org/10.1016/j.jhydrol.2019.123923.

Wei, Z., Lee, X., Aemisegger, F., Benetti, M., Berkelhammer, M., Casado, M., Caylor, K., Christner, E., Dyroff, C., García, O., González, Y., Griffis, T., Kurita, N., Liang, J., Liang, M.C., Lin, G., Noone, D., Gribanov, K., Munksgaard, N.C., Schneider, M., Ritter, F., Steen-Larsen, H.C., Vallet-Coulomb, C., Wen, X., Wright, J.S., Xiao, W., Yoshimura, K., 2019. A global database of water vapor isotopes measured with high temporal resolution infrared laser spectroscopy. Sci. Data 6, 1–15. https://doi.org/10.1038/sdata.2018.302.

Wei, Z., Yoshimura, K., Okazaki, A., Kim, W., Liu, Z., Yokoi, M., 2015. Partitioning of evapotranspiration using high-frequency water vapor isotopic measurement over a rice paddy field. Water Resour. Res. https://doi.org/10.1002/2014WR016737.

Wei, Z., Yoshimura, K., Wang, L., Miralles, D.G., Jasechko, S., Lee, X., 2017. Revisiting the contribution of transpiration to global terrestrial evapotranspiration. Geophys. Res. Lett. 44, 2792–2801. https://doi.org/10.1002/2016GL072235.

Welker, J.M., 2012. ENSO effects on $\delta^{18}O$, δ^2H and D-excess values in precipitation across the U.S. using a high-density, long-term network (USNIP). Rapid Commun. Mass Spectrom. 26, 1893–1898. https://doi.org/10.1002/rcm.6298.

Welker, J.M., 2000. Isotopic ($\delta^{18}O$) characteristics of weekly precipitation collected across the USA: an initial analysis with application to water source studies. Hydrol. Process. 14, 1449–1464. https://doi.org/10.1002/1099-1085(20000615)14:8<1449::AID-HYP993>3.0.CO;2-7.

Welp, L.R., Lee, X., Griffis, T.J., Wen, X.F., Xiao, W., Li, S., Sun, X., Hu, Z., Val Martin, M., Huang, J., 2012. A meta-analysis of water vapor deuterium-excess in the midlatitude atmospheric surface layer. Glob. Biogeochem. Cycl. 26, 1–12. https://doi.org/10.1029/2011GB004246.

Welp, L.R., Lee, X., Kim, K., Griffis, T.J., Billmark, K.A., Baker, J.M., 2008. $\delta^{18}O$ of water vapour, evapotranspiration and the sites of leaf water evaporation in a soybean canopy. Plant, Cell Environ. 31, 1214–1228. https://doi.org/10.1111/j.1365-3040.2008.01826.x.

Werner, C., Schnyder, H., Cuntz, M., Keitel, C., Zeeman, M.J., Dawson, T.E., Badeck, F.W., Brugnoli, E., Ghashghaie, J., Grams, T.E.E., Kayler, Z.E., Lakatos, M., Lee, X., Máguas, C., Ogée, J., Rascher, K.G., Siegwolf, R.T.W., Unger, S., Welker, J., Wingate, L., Gessler, A., 2012. Progress and challenges in using stable isotopes to trace plant carbon and water relations across scales. Biogeosciences 9, 3083–3111. https://doi.org/10.5194/bg-9-3083-2012.

Wilson, K., Goldstein, A., Falge, E., Aubinet, M., Baldocchi, D., Berbigier, P., Bernhofer, C., Ceulemans, R., Dolman, H., Field, C., Grelle, A., Ibrom, A., Law, B.E., Kowalski, A., Meyers, T., Moncrieff, J., Monson, R., Oechel, W., Tenhunen, J., Valentini, R., Verma, S., 2002. Energy balance closure at FLUXNET sites. Agric. For. Meteorol. https://doi.org/10.1016/S0168-1923(02)00109-0.

Winnick, M.J., Chamberlain, C.P., Caves, J.K., Welker, J.M., 2014. Quantifying the isotopic "continental effect. Earth Planet. Sci. Lett. 406, 123–133. https://doi.org/10.1016/j.epsl.2014.09.005.

Worden, J., Bowman, K., Noone, D., Beer, R., Clough, S., Eldering, A., Fisher, B., Goldman, A., Gunson, M., Herman, R., Kulawik, S.S., Lampel, M., Luo, M., Osterman, G., Rinsland, C., Rodgers, C., Sander, S., Shephard, M., Worden, H., 2006. Tropospheric Emission Spectrometer observations of the tropospheric HDO/H2O ratio: estimation approach and characterization. J. Geophys. Res. Atmos. 111, 1–10. https://doi.org/10.1029/2005JD006606.

Worden, J., Noone, D., Bowman, K., Beer, R., Eldering, A., Fisher, B., Gunson, M., Goldman, A., Herman, R., Kulawik, S.S., Lampel, M., Osterman, G., Rinsland, C., Rodgers, C., Sander, S., Shephard, M., Webster, C.R., Worden, H., 2007. Importance of rain evaporation and continental convection in the tropical water cycle. Nature 445, 528–532. https://doi.org/10.1038/nature05508.

Wright, C.K., Wimberly, M.C., 2013. Recent land use change in the Western Corn Belt threatens grasslands and wetlands. Proc. Natl. Acad. Sci. U. S. A. 110, 4134–4139. https://doi.org/10.1073/pnas.1215404110.

Xia, Y., Hobbins, M.T., Mu, Q., Ek, M.B., 2015. Evaluation of NLDAS-2 evapotranspiration against tower flux site observations. Hydrol. Process. 29, 1757–1771. https://doi.org/10.1002/hyp.10299.

Xia, Z., Winnick, M.J., 2021. The competing effects of terrestrial evapotranspiration and raindrop re-evaporation on the deuterium excess of continental precipitation. Earth Planet. Sci. Lett. 572, 117120 https://doi.org/10.1016/j.epsl.2021.117120.

Xiao, W., Wei, Z., Wen, X., 2018. Evapotranspiration partitioning at the ecosystem scale using the stable isotope method—a review. Agric. For. Meteorol. 263, 346–361. https://doi.org/10.1016/j.agrformet.2018.09.005.

Yakir, D., Wang, X.F., 1996. Fluxes of CO2 and water between terrestrial vegetation and the atmosphere estimated from isotope measurements. Nature 380, 515–517. https://doi.org/10.1038/380515a0.

Yebra, M., Dijk, A.Van, Leuning, R., Huete, A., Pablo, J., 2013. Remote Sensing of Environment Evaluation of optical remote sensing to estimate actual evapotranspiration and canopy conductance. Remote Sens. Environ. 129, 250–261. https://doi.org/10.1016/j.rse.2012.11.004.

Zangvil, A., Portis, D.H., Lamb, P.J., 2004. Investigation of the large-scale atmospheric moisture field over the midwestern United States in relation to summer precipitation. Part II: recycling of local evapotranspiration and association with soil moisture and crop yields. J. Clim. 17, 3283–3301. https://doi.org/10.1175/1520-0442(2004)017<3283:IOTLAM>2.0.CO;2.

Zeng, Z., Peng, L., Piao, S., 2018. Response of terrestrial evapotranspiration to Earth's greening. Curr. Opin. Environ. Sustain. 33, 9–25. https://doi.org/10.1016/j.cosust.2018.03.001.

Zhang, W., Furtado, K., Wu, P., Zhou, T., Chadwick, R., Marzin, C., Rostron, J., Sexton, D., 2021. Increasing precipitation variability on daily-to-multiyear time scales in a warmer world. Sci. Adv. 7, 1–12. https://doi.org/10.1126/sciadv.abf8021.